ISTANBUL TECHNICAL UNIVERSITY ★ GRADUATE SCHOOL

3D-Printed Actuator-Based Beam-Steering Approach for Improved Physical Layer Security in Visible Light Communication

M.Sc. THESIS

Mehmet Can ERDEM

Department of Electronics and Communication Engineering

Electronics Engineering Programme

SEPTEMBER 2022

ISTANBUL TECHNICAL UNIVERSITY ★ GRADUATE SCHOOL

3D-Printed Actuator-Based Beam-Steering Approach for Improved Physical Layer Security in Visible Light Communication

M.Sc. THESIS

Mehmet Can ERDEM
(504201223)

Department of Electronics and Communication Engineering

Electronics Engineering Programme

Thesis Advisor: Doç. Dr. Onur FERHANOĞLU

SEPTEMBER 2022

İSTANBUL TEKNİK ÜNİVERSİTESİ ★ LİSANSÜSTÜ EĞİTİM ENSTİTÜSÜ

Görünür Işıkla Haberleşmede Geliştirilmiş Fiziksel Katman Güvenliği için 3D Baskılı Aktüatör Tabanlı Işın Hüzmesinin Yönlendirilmesi Tekniği

YÜKSEK LİSANS TEZİ

Mehmet Can ERDEM
(504201223)

Elektronik ve Haberleşme Mühendisliği Anabilim Dalı

Elektronik Mühendisliği Programı

Tez Danışmanı: Doç. Dr. Onur FERHANOĞLU

EYLÜL 2022

Mehmet Can ERDEM, a M.Sc. student of ITU Graduate School student ID 504201223, successfully defended the thesis entitled “3D-Printed Actuator-Based Beam-Steering Approach for Improved Physical Layer Security in Visible Light Communication”, which he/she prepared after fulfilling the requirements specified in the associated legislations, before the jury whose signatures are below.

Thesis Advisor : **Doç. Dr. Onur FERHANOĞLU** ....
Istanbul Technical University

Jury Members : **Dr. Öğr. Üyesi Ahmet Can ERTEN** ....
Istanbul Technical University

Doç. Dr. Yiğit Dağhan GÖKDEL ....
Istanbul Bilgi University

Date of Submission : 19 August 2022
Date of Defense : 5 September 2022

To my family,

FOREWORD

This thesis was written in line with my master's degree in the Electronics Engineering program of Istanbul Technical University. It was also conducted as a part of a TÜBİTAK (The Scientific and Technological Research Institution of Turkey) project titled "Physical Layer Security in Visible Light Communication", with the number 218E034. Furthermore, this thesis was published in the Applied Optics journal of Optica, on June 13th, 2022. For my thesis, I would like to thank my parents and the other members of my family for their unwavering support in my education and research work. I would like to thank my thesis supervisor Assoc. Prof. Onur Ferhanoğlu for his guidance and support, while I would like to thank Prof. Güneş Karabulut Kurt from Polytechnique Montréal and Prof. Erdal Panayırcı from Kadir Has University for their assistance. I would also like to thank Oğuz Gürcüoğlu and other members of the Electro-Optical Devices Laboratory for their assistance and support.

September 2022 Mehmet Can ERDEM

TABLE OF CONTENTS

Page

ABBREVIATIONS

3D	: Three-Dimensional
App	: Appendix
BW	: Bandwidth
CAD	: Computer-Aided Design
CCD	: Charge-Coupled Device
CMOS	: Complementary Metal–Oxide–Semiconductor
FDM	: Fused Deposition Modeling
FEA	: Finite Element Analysis
LED	: Light-Emitting Diode
Li-Fi	: Light Fidelity
MEMS	: Micro-Electro-Mechanical Systems
MISO	: Multiple-Input Single-Output
NA	: Numerical Aperture
NEP	: Noise-Equivalent Power
PD	: Photo-detector
pix	: Pixel
PLA	: Polylactic Acid
SNR	: Signal-to-Noise Ratio
STL	: Standard Triangle Language
VLC	: Visible Light Communication

SYMBOLS

$\mathbf{C_s}$	: Secrecy capacity
D	: Lens diameter
d	: Density
E	: Young's modulus
h	: Frame height
$\mathbf{h_f}$	: Flexure height
$\mathbf{h_{lens}}$	: Lens holder height
$\mathbf{k_x, k_y, k_z}$	: Spring constants in x, y and z-directions
$\mathbf{L_f}$	: Flexure length
$\mathbf{t_f}$	: Flexure thickness
$\mathbf{V_x, V_y}$	: Voltage applied in x and y-directions
$\mathbf{w_f}$	: Flexure width
W	: Frame width and length
$\mathbf{W_{lens}}$	: Lens holder width
$\boldsymbol{\lambda}$	: Wavelength

LIST OF TABLES

Page

LIST OF FIGURES

Page

3D-Printed Actuator-Based Beam-Steering Approach for Improved Physical Layer Security in Visible Light Communication

SUMMARY

In this thesis, the design, manufacturing and implementation of a 3D-printed lens scanner-based beam-steering are presented for use in visible light communication (VLC) applications. The scanner, measuring 5 x 5 cm, is designed for low-cost 3D printing with fused deposition modeling using polylactic acid (PLA). The scanning is facilitated through electromagnetic actuation of the lens frame, carrying a conventional 25 mm lens in two nearly orthogonal directions. The serpentine spring that connects the lens frame to the external frame is tailored to offer similar spring constants in the directions of actuation, and minimal (< 1.5 mm) sag due to the mass of the lens. The manufactured actuator was integrated on a miniaturized VLC test-bed (70 cm x 40 cm x 40 cm).

Using the test-bed, the applied voltage vs. beam displacement behavior of the actuator was characterized in the lateral plane, and beam-steering on a moving target was demonstrated with face-recognition feedback. The proposed scheme was targeted to offer an improved security measure in VLC through tracking the legitimate receiver (i.e. via face recognition) and using the feedback to steer the focused light onto the targeted device. The joint use of focusing and steering features allows for the legitimate receiver to roam within the room while enjoying the improved secrecy due to focused light. The secrecy capacity for the demonstrated approach was also calculated, which compares favorably to a number of jamming, spatial modulation and beam-forming counterparts.

The presented actuator can be used with larger room dimensions, yet up-scaling to larger illumination units will require the use of a lens having a smaller focus to achieve a larger total steering angle.

This thesis is composed of five different chapters. The concepts of visible light communication and light fidelity (Li-Fi) are introduced with a thorough literature review in the first chapter, while the techniques used in the thesis are also defined and presented. In the second chapter, the design of the actuator is described through definite computer-aided design (CAD) models and finite element analysis (FEA) simulations, while the experimental setup is also presented. Meanwhile, the demonstrations and the measurement results from the beam-steering operation of the actuator are presented in the third chapter. Then, the discussion section, based on the secrecy improvement through the use of the actuator and the upscaling of the actuator

to real-world dimensions, is presented in the fourth chapter. Finally, the fifth chapter presents the conclusions and further future work based on the actuator.

Görünür Işıkla Haberleşmede Geliştirilmiş Fiziksel Katman Güvenliği için 3D Baskılı Aktüatör Tabanlı Işın Hüzmesinin Yönlendirilmesi Tekniği

ÖZET

Bu çalışmada, görünür ışıkla haberleşme (VLC) uygulamaları için daha gelişmiş bir fiziksel katman güvenliği sağlamak amacıyla bir 3 boyutlu yazıcı ile oluşturulmuş bir lens tarayıcısının tasarımı, üretimi ve ışın hüzmesinin yönlendirilmesi tekniği ile yapılan deneyler betimlenmiştir. Bu lens tarayıcısı, 5 x 5 cm boyutlarında olup polilaktik asit (PLA) materyaliyle ve FDM (fused deposition modelling/eriyik yığma modelleme) tekniğiyle tasarlanmıştır. Betimlenen bu tarama işlemi, 25 mm çaplı bir lensi taşıyan lens çerçevesinin üzerinde bulunan iki neodimyum mıknatıs ile tarayıcının dış çerçevesinin içerisinde bulunan iki bobin arasındaki elektromanyetik etkileşimler ile yapılmıştır. Mıknatıslar, lens çerçevesinin sağ üst kısmında x ile y eksenlerinde ve birbirlerine göre dik açılı olacak şekilde, bobinler ise dış çerçevenin sağ üst kısmında ve mıknatısların tam olarak karşılarında bulunacak şekilde yerleştirilmiştir. Lens çerçevesini dış çerçeveye bağlayan kıvrımlı yay yapısı, x ile y eksenlerinde benzer yay sabitleri olacak şekilde ve merceğin kütlesi sonucu minimum bir sarkma (< 1,5 mm) sağlayacak şekilde tasarlanmıştır. Üretilen eyleyici, minyatür bir VLC test yatağına (70 cm x 40 cm x 40 cm) entegre edilmiştir.

Oluşturulan bu lens tarayıcısı için belirtilen VLC test yatağı içerisinde bobinlere 10 Volt'a kadar çeşitli farklı değerlerde gerilim uygulanması ile bir LED içerisinden çıkan ışın hüzmesinin yere düşen ana lobunun değişik gerilim değerlerine göre yer değiştirmesi karakterize edilmiştir. Bununla birlikte, yapılan bu yer değiştirme işlemleri ile bir yüz tanıma programının kullanımı sayesinde hareketli bir hedef üzerinde ışın hüzmesinin yönlendirilmesi betimlenmiştir. Bu çalışmada önerilen güvenlik şeması, bir yüz tanıma programı ile meşru alıcının oda içerisinde hareketlerini izleyerek VLC için daha gelişmiş bir fiziksel katman güvenliği sağlamıştır. Işın hüzmesinin meşru alıcı üzerinde odaklanması ve yönlendirilmesi teknikleri, betimlenen bu sistemin kullanımı ile birlikte meşru alıcının oda içinde serbestçe dolaşmasına izin vermektedir ve alıcının verilerinin odada bulunabilecek diğer dinleyicilere karşı daha korunaklı olmasını sağlamaktadır. Ayrıca, belirtilen bu sistemin gizlilik kapasitesi hesaplanmıştır ve alınan sonuçlar, başka benzer çalışmalar ile de karşılaştırılmıştır.

Tasarlanan eyleyici daha büyük boyutlara sahip olacak şekilde oluşturulup daha büyük bir oda içerisinde kullanıma sunulabilir, ancak daha büyük aydınlatma birimleri ile ışın hüzmelerinin yönlendirilmesini sağlamak amacıyla daha büyük bir toplam yönlendirme açısının elde edilmesi gerekmektedir. Bu sebepten dolayı da eyleyici

içerisinde daha küçük odaklı bir lensin kullanılması gerekir.

Bu çalışma, beş ayrı bölümden oluşmaktadır. Birinci bölümde, görünür ışıkla haberleşme ve ışık tabanlı bağlantı (Li-Fi) kavramları kapsamlı bir literatür taraması ile tanıtılırken, tezde kullanılan çeşitli teknikler ve önerilen fiziksel katman güvenlik şeması tanımlanıp bu bölümde sunulmuştur. İkinci bölümde, belirli bilgisayar destekli tasarım (CAD) modelleri ve sonlu elemanlar analizi (FEA) simülasyonları ile eyleyicinin tasarımı ile üretimi anlatılmıştır ve deney düzeneği ile birlikte sunulmuştur. Üçüncü bölümde, eyleyicinin ışın hüzme yönlendirme işleminden elde edilen ölçüm sonuçları ve çeşitli deneyler sunulmuştur. Dördüncü bölümde, eyleyicinin kullanımı yoluyla gizlilik kapasitesinin arttırılmasına ve eyleyicinin gerçek hayattaki uygulamalarda kullanılabilmesi için boyutlarının ve kullandığı çeşitli komponentlerin değiştirilmesine dayanan tartışma bölümü sunulmuştur. Beşinci ve son bölümde ise, oluşturulan eyleyiciye dair çeşitli çıkarımlar ve sonuçlar belirtilmiştir.

1. INTRODUCTION

In the first chapter of the thesis, the concepts of visible light communication (VLC) and light fidelity (Li-Fi) are introduced with a thorough literature review, while the concept of physical layer security in VLC and the techniques used in the thesis are also defined and explained. These techniques are essential in the design of the actuator and the measurement phase of the experiment. Meanwhile, the proposed improved physical layer security scheme for a VLC Li-Fi configuration will also be explained in this chapter.

1.1 Visible Light Communication (VLC)

Visible light communication, known by its abbreviation, VLC, is a type of optical wireless data communication that utilizes the visible light spectrum as a medium in order to transmit or receive signals inside a confined area [4]. The visible light spectrum used by VLC consists of a wavelength range of approximately 380 to 750 nm. Thus, VLC offers short-range optical communication through visible light modulation in both indoor and outdoor environments [4].

Data communication under visible light is generally conducted by a light source to transmit the signal of interest and a photo-detector to capture and receive this signal to finalize the data transfer. The light sources that can be used for VLC vary from simple LEDs (light-emitting diodes) to standard lamps, while the photo-detectors can vary from photo-diodes to image sensors and standard cameras.

VLC can be utilized in many significant areas that integrate optics and electronics. Video surveillance, Li-Fi, robotics, and other point-to-point communication systems can be counted as some of the applications of VLC [5]. Also, offering a large bandwidth, employing already existing illumination, and not causing interference with consumer electronic products, VLC is considered a promising complement to radio frequency (RF) communication [6].

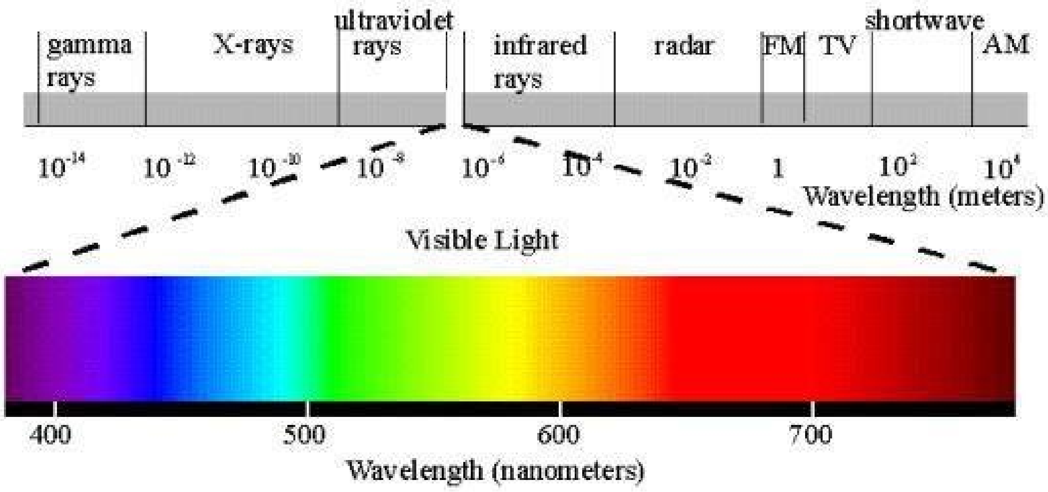

Figure 1.1 : The visible light spectrum [1].

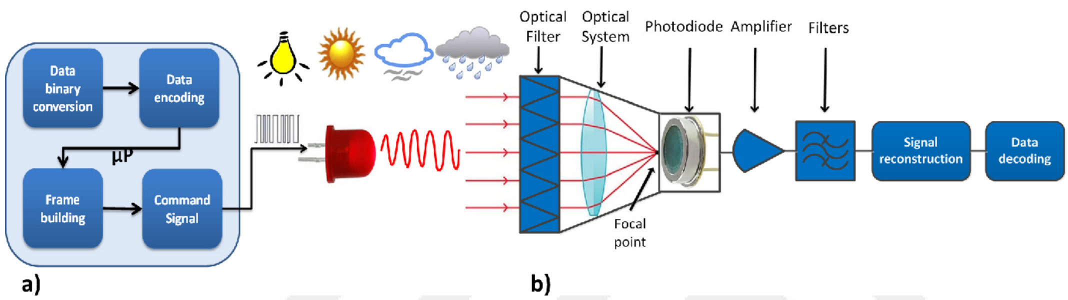

Figure 1.2 : A sample VLC process, depicting the data communication between a LED source and a photo-diode recipient. (a) denotes the encoding process of the data to be transmitted through the optical medium, while (b) depicts the reception of the data that is delivered to the recipient [2].

1.1.1 The main processes of VLC

As depicted in Figure 1.2, the main principle of VLC is to take encoded data, process this data into an electrical signal using a driver, and deliver this signal into the visible light medium using a light source [7]. Several techniques, such as beam-forming and beam-steering, or definite algorithms can be employed to direct the light in this medium without the necessity of changing the characteristics of the signal. Inside this medium, the directed light will be received by designated optical structures and systems, which will focus the light onto the recipient light sensor. The recipient sensor will then convert this signal into an electrical output, which would then be decoded into the data of interest at the end of the process [7].

1.1.2 The main advantages, disadvantages and applications of VLC

With its main processes explained, it can be said that the main advantages of VLC are considered to be its large bandwidth and low power consumption [6]. Light sources, such as LEDs, provide a larger bandwidth limitation than that of the RF antennas. In the meantime, VLC is assigned for both illumination and communication inside the designated space, which makes it more power-efficient in terms of the assignments that it does [6].

However, perhaps the main disadvantage of VLC is that it is mainly required for this type of data communication to be held in a confined space without any interference from other ambient light sources, light sensors, or further intrusion on the light medium inside this environment [4]. Despite this issue, it can be said that VLC can be used for many applications that are established in the technology of today. Several notable examples can be considered as Li-Fi, robotics, vehicle-to-vehicle communication, underwater communication, video surveillance, traffic management, and further point-to-point communication systems [5].

1.2 Light Fidelity (Li-Fi)

Light fidelity, also known as Li-Fi, is a wireless optical communication technology that is based on the transmission of data using visible light between definite devices of interest that are located in a confined space [8]. Li-Fi can also be regarded as an improved version of VLC, where the original point-to-point data transmission of VLC is improved into a multi-point wireless technology between devices in Li-Fi, conducted with visible light. The data transmission in Li-Fi is conducted through the use of LED bulbs, while the data transmission rate can be controlled through the mapping of a set of encoded data onto different levels of beam intensities. As an example, a sample of binary data can be mapped onto designated low and high rates of beam intensities, for the 0 and 1 bits, respectively. Therefore, the encoded data is transmitted from the LED bulbs to the recipient sensors with the use of specific optical techniques, structures, or algorithms. Lastly, the received data is decoded at the end of the depicted circuit and prepared for further use.

For the data transmission, various modulation schemes can be employed to manage the ON-OFF shift of the LEDs, which consist of mainly single carrier-based schemes [8]. On-off keying (OOK), pulse width modulation (PWM), pulse position modulation (PPM), and optical spatial modulation (OSM) can be regarded as some of the examples of these single carrier-based modulation schemes. These modulation schemes can be utilized through different sets of algorithms, while some circuit components can also be employed to conduct the modulation of the intensity of the light beams, such as spatial light modulators (SLM).

Overall, it can be stated that Li-Fi can offer a higher level of security, accuracy, bandwidth, data density, and cost-efficiency than Wi-Fi [9]. As Li-Fi is confined by certain physical barriers and reach, it also gains an advantage against interference and intrusions that Wi-Fi technology cannot overcome. The use of the light spectrum, which consists of visible light and sometimes certain parts of the IR (infrared) and UV (ultraviolet) light spectra, also provides certain advantages for Li-Fi in the bandwidth of the communication, making the capacity of the overall spectrum 10,000 times larger than the radio waves. Furthermore, Li-Fi can offer a data rate that can reach 10 to 15 Gbps (Gigabits per second), and it also employs a simple and cost-efficient LED lighting system to establish the communication [9].

1.3 Security Issues and Physical Layer Security in VLC

As previously stated, the main disadvantage of VLC is the necessity of conducting data communication in a confined space. Due to this situation, VLC is prone to be meddled with by external interference targeting the data itself or its transfer in the light medium. Therefore, while VLC is a good alternative to be utilized for wireless data communication in several aspects, it can be stated that there are several security issues with VLC. In order to provide some examples regarding these security issues, there can be discussed the aspects of jamming, eavesdropping, and data modification [10].

Regarding jamming, it can be said that it is related to the range of the data transmission across the light medium where a blockage or interference on the data transfer can occur, proportional to this range [10]. Meanwhile, the aspect of eavesdropping is related to the transmission power and area of influence, where the security risk of snooping on the data increases proportionally to these parameters [10]. Lastly, the aspect of data modification is both related to the range and the area of influence, where it becomes possible to meddle with and possibly change the data that is being transferred along the light medium [10].

Due to these possible security risks, it is important to constantly inspect and perhaps oversee the data transfer in the VLC network for further inductions and possible solutions. Therefore, these security issues in VLC are of utmost importance. These issues must be addressed in order to increase the feasibility of such systems for practical applications. The concept of physical layer security aims to study the physical characteristics of wireless channels, based on the fundamental information-theoretical security framework proposed by Shannon [11] and Wyner [12], which is utilized to establish sturdy links between the transmitter (i.e. Alice) and legitimate receivers (i.e. Bob) while preventing any illegitimate receivers (eavesdroppers, i.e. Eve) from obtaining any necessary data over the channel [13].

A number of techniques have been developed in the area of physical layer security, such as beam-steering using acousto-optic deflectors [14], pre-coding based spatial modulation [15], and optical beam-forming [16] [17]. Friendly jamming has been proposed as a secure strategy in single and multiple transmitter systems, employing null-steering, production of artificial noise, and beam-forming to improve secrecy rates on the legitimate receiver [18]. Meanwhile, another research has demonstrated the use of optical lenses in front of a selected transmitter to enhance the VLC link secrecy on a multiple-input single-output (MISO) VLC system, where the spatial distribution of the light is limited to a secure region [19].

1.4 Optical Beam-steering

In order to define the optical beam-steering technique, a brief introduction to the concept of beam-steering should also be provided. Beam-steering can be defined as focusing and directing the main lobe of the radiation generated by a certain energy source towards the desired location by changing its shape and targeted destination in certain ways. Originally, this concept was formulated in the beam-forming technique, which utilizes the constructive and destructive interference caused by the emitted electromagnetic wave radiation in order to form the main lobe of the radiation.

The most important feature of the beam-steering technique is the ability to control and change the location of the main lobe of the resulting radiation pattern in real-time. While the beam-forming technique is only used to collect the scattered rays from the energy source onto a certain location, the beam-steering technique is used to direct the beams onto different focused locations of interest without the need to reconstruct the main lobe each time. This process can be conducted with certain algorithms, systems, or definite auxiliary components. Therefore, the beam-steering technique can also be regarded as an improved version of the beam-forming technique. These two techniques are regularly used for various communication purposes, mainly in RF applications. For applications in communication, the main benefits of the beam-steering technique include the reduction of any possible interference in the data transmission using the beams and the increase in the spectral efficiency through the increase in the SNR (signal-to-noise ratio) of the data transmission.

Therefore, in optical beam-steering; various optical components, devices, and several optical techniques are used in order to control and guide the beams from a light source towards a designated location during the data transmission in the light medium. Signal processing algorithms, changing the refractive index of the light medium, and changing the direction and position of the beams can be specified as some of the techniques that can be utilized for this purpose. For instance, lenses, such as collimators, reflectors and deflectors, are used to control and direct the scattered beams. In several applications, actuator structures are also employed to configure and maintain the overall process.

1.4.1 Optical beam-steering in Li-Fi

Optical beam-steering can therefore be considered an example of the techniques that can be used to improve the physical layer security in VLC. A sample Li-Fi setup is provided in Figure 1.2, as an example of the use of optical beam-steering [3]. In this configuration, a LED array is placed on the ceiling of the room, connected to a micro-controller and a spatial light modulator (SLM). Firstly, the positions of the devices that are present in the room, are determined using the position sensors that are connected to the micro-controller. Then, visible light communication is initiated between the LED array and the devices that are detected to be present in the room. The beam-forming is achieved by formulating and combining the main lobes of the beams

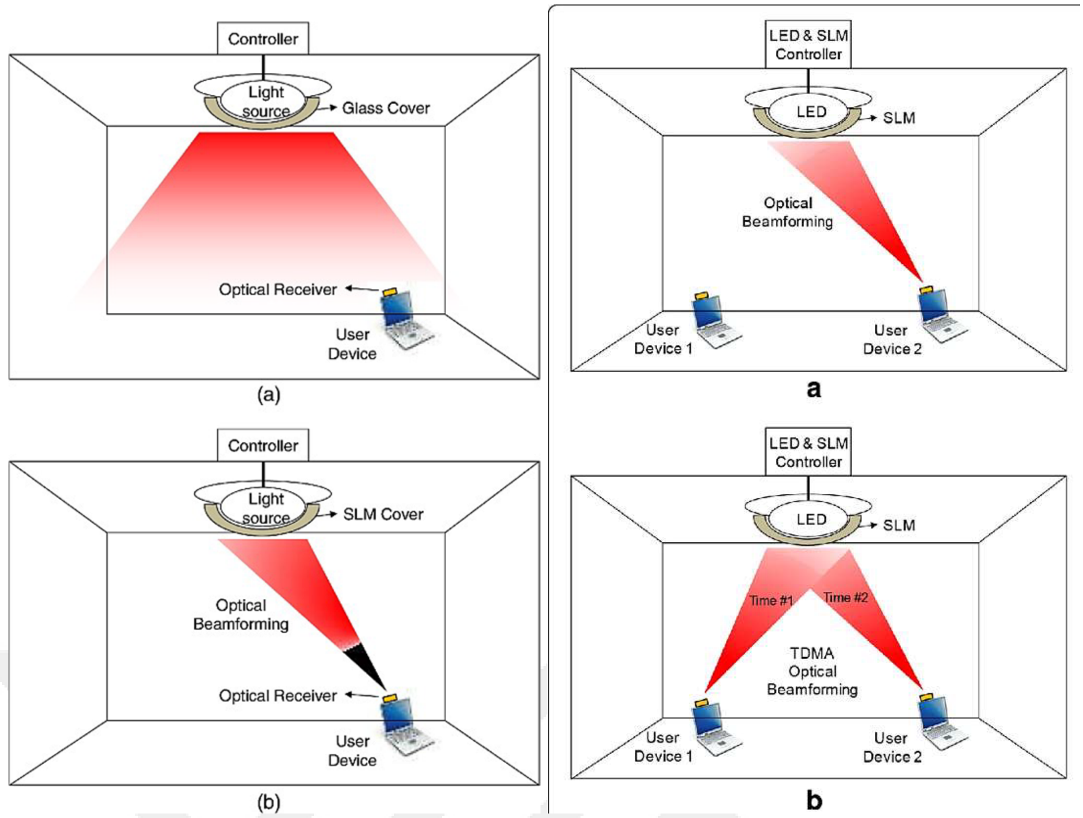

Figure 1.3 : A depiction of a sample scenario about optical beam-forming in a) and beam-steering in b) in different time intervals between the LED array and the devices in the room via VLC. [3]

created by the LEDs towards the designated location of a device. Also, as indicated in Figure 1.2-b), it is possible to steer the main lobe onto different devices at different time intervals. This technique allows the main lobe to change its position on the floor of the room, where it depends on designated sets of different time interval values.

1.5 The Proposed Physical Layer Security Scheme

Thanks to its rapid and low-cost manufacturing capability (both equipment and filament cost) and low price, 3D printing has emerged as an alternative technique for micro-system manufacturing [20]. Micro-electro-mechanical system (MEMS) based lens scanners were presented comprising hybrid structures with multiple bonded devices for lateral and axial scanning and devices with deformable surfaces for focus adjustment in combination with lateral scanning devices [21] [22]. However, MEMS-based solutions also comes with fabrication complexity and a limited displacement range. Figure 1.3 illustrates the proposed physical layer security

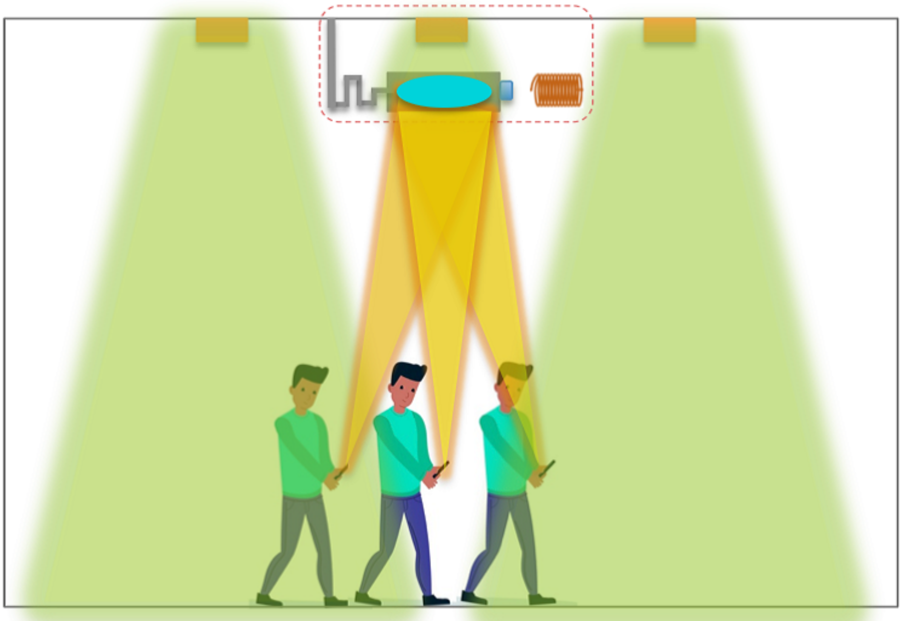

Figure 1.4 : The proposed physical security scheme for visible light communication, which is composed of an electromagnetic actuator placed in front of a selected transmitter to follow the legitimate receiver.

scheme. The proposed physical layer security scheme utilizes an electromagnetic actuator-based lens scanner that is configured to conduct optical beam-steering onto the current location of the receiver of the VLC system, in order to provide a more secure data communication between the LED light source and the receiver.

A design review of the actuator is provided in the following section, along with the experimental setup for the demonstration of optical beam-steering on a moving target based on face recognition feedback.

1.6 Fused Deposition Modeling (FDM)

Fused deposition modeling (FDM) is one of the most prominent types of additive manufacturing techniques, which is used to create solid models, patterns and more complex parts with delicate geometries using formulated computer-aided design (CAD) drawings. FDM employs the use of an extrusion nozzle, where a thermoplastic material is melted down by a heated extruder that is located inside. The molten thermoplastic material is then deposed by the nozzle onto the top of a building platform that generally consists of a glass surface. The patterns of the design of interest are constructed layer by layer on top of each other, where these layers are fused together to build up the desired three-dimensional object. FDM is generally advantageous in terms of its ability to use a wide range of materials, cost-effectiveness, reliability and durability. With these features, it can be stated that FDM is one of the most convenient techniques used in 3D printing.

1.7 Facial Detection and Recognition

The main elements that were used to construct the program necessary for the experiment stated in the thesis were the face detection and face recognition algorithms. Face detection algorithms are used to detect human frontal faces in an image or a video, where these images or videos are compared with a pre-defined image data set in order to find and depict facial features that belong to a person. Meanwhile, face recognition algorithms are used to declare who the person is after comparing these images or videos with the pre-defined data set.

2. DESIGN OF THE ACTUATOR

2.1 Design Specifications of the Actuator

The designed lens scanner, illustrated in Figure 2.1, comprises a serpentine flexure connected to a lens frame holding a 25 mm diameter (f = 25 mm) plano-convex lens. The outer frame size is set to 5 cm x 5 cm, which is half the period in which the LEDs are placed in the miniaturized VLC test-bed. Two Neodymium magnets (3 mm diameter, 1 mm thick) were placed at the distal edge and distal corner to facilitate electromagnetic actuation. Coil slots were defined on the outer frame, across the magnets, to establish electromagnetic force in two different directions. Two 6-mm diameter vias were defined on the outer frame as a means to insert opto-mechanical cage rods for the integration of the scanner with the test-bed. The dimensions of the designed scanner are provided in Table 2.1. It is noteworthy to mention that the choice of using a one-sided serpentine spring over one or multiple guided beams relies on decreasing the spring constant to a level that will result in near 1 mm in x and y directions using the utilized coil and 10 V drive voltage.

Table 2.1 : The dimensions of the designed lens scanner.

Feature	Symbol	Size
Frame width and length	W	50 mm
Lens holder width	W_{lens}	30 mm
Flexure length	L_f	11 mm
Frame height	h	15 mm
Lens holder height	h_{lens}	10 mm
Flexure height	h_f	10 mm
Flexure width	w_f	30 mm
Flexure thickness	t_f	1 mm
Flexure gap thickness	t_g	1 mm
Lens diameter	D	25 mm

The CAD drawings are as depicted in Figure 2.1. These CAD drawings were created with the AutoCAD software, while Figure 2.1. also depicts a comparison between the drawings and the manufactured result for the actuator.

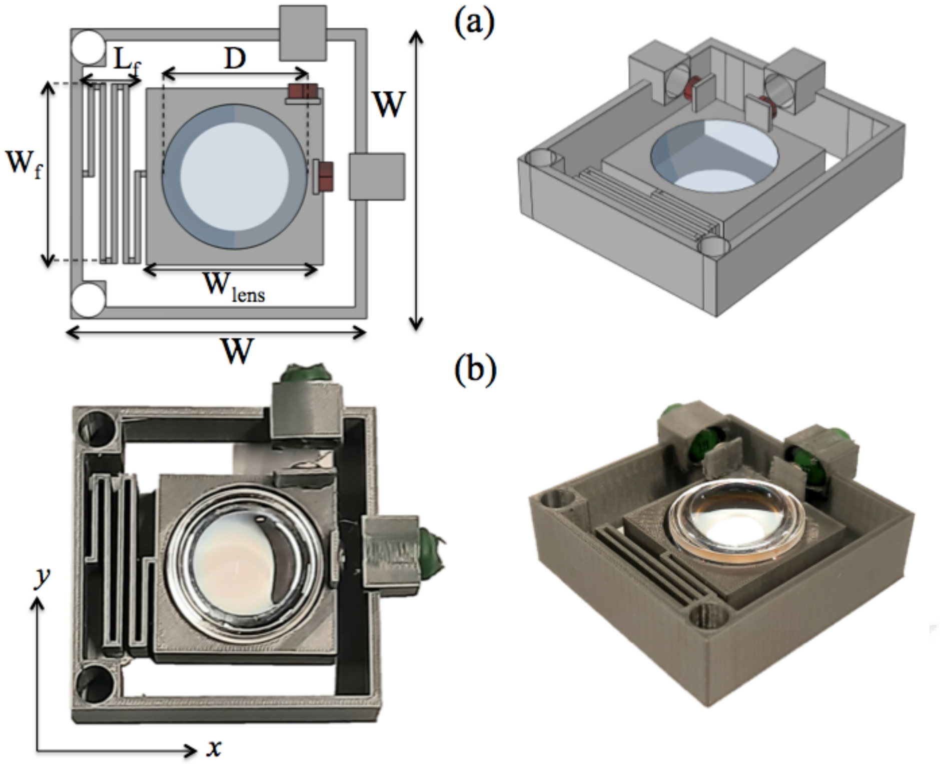

Figure 2.1 : Designed 3D-printed scanner; two different views from a) the CAD drawing and b) the manufactured device.

The flexure width, length and number of serpentine periods were adjusted within the manufacturing limit to minimize the spring constant in three dimensions while ensuring tolerable sag of the lens due to gravity. In the lateral plane, the spring constant in the horizontal direction (k_x) can be modeled using a serial combination of 5 vertical cantilevers (2 of the cantilevers having a length of half the flexure width, and 3 of them having a length of full flexure width W_f), which the 2-period serpentine is composed of), such that [23]:

$$k_x = \left(\frac{2}{(E * h_f * t_f^3/(W_f/2)^3)} + \frac{3}{(E * h_f * t_f^3/(W_f)^3))}\right)^{-1} \quad \mathbf{(2.1)}$$

where E is the Young's modulus of polylactic acid (PLA), and the other parameters are as summarized in Table 1.

The manufacturing of the actuator with FDM was followed by the press-fit placement of the 25-mm focal length lens and two 100 mH inductor coils. The neodymium magnets were attached to the rectangular prism features defined on the lens frame edge and the corner using standard epoxy. The coil–magnet distance was kept closer in the x-direction than in the y-direction to compensate for the difference in spring constants and to obtain a similar sensitivity in displacement vs. voltage behavior.

In order to formulate the final prototype of the actuator, many different types of designs were produced and tested in order to create the final result. These designs were gradually updated depending on the observations made during the design and the experiment phases, which shaped the final result provided in Figure 2.1. The improvements in the design of the actuator are discussed in Section 4.2. and several figures for the earlier versions of the actuator are provided in Appendix B.

2.2 Design Simulations of the Actuator

2.2.1 The FEA simulations for the k spring constants

Several finite element analysis (FEA) simulations based on the design of the actuator were conducted in the COMSOL Multiphysics software. These simulations consist of the static deflection simulations, which are based on the k spring constants from Hooke's law in three dimensions, and the von Mises stress simulation, which determines if the constructed flexure under a definite load will yield, deform or fracture, depending on the load. In the FEA simulations, the mechanical properties were utilized in accordance with the PLA manufacturer's specifications (E = 3.5 GPa, density : d = 1240 kg/m^3).

The FEA results for the k spring constants of the flexure of the actuator are presented in Figure 2.2, where a static force of 0.1 N was applied in the lateral directions (x and y) and 0.15 N in the z (perpendicular) direction, mimicking the weight of the frame (total of lens weight and the PLA holder section). The spring constant in the horizontal direction was deduced to be k_x = 369 N/m from FEA, which is in line with the stiffness found from analytical formulation (398 N/m) based on Equation 2.1. FEA revealed a compliant stiffness in the y-direction k_y = 65 N/m when observed from the center of the lens. Moreover, the vertical stiffness of k_z = 110 N/m, reveals a < 1.5mm sag at the lens center, ensuring minimal misalignment between the magnets and the coils when the actuator is loaded with the lens.

Meanwhile, it can be said that some information based on the resonance of the structure can also be provided from the obtained values from the simulations. The fundamental mechanical resonant frequency (f_m) of the lens scanner in its current form can be calculated from its spring constants (k) and mass (m) as:

$$f_m = \frac{1}{2\pi}\sqrt{\frac{k}{m}} \tag{2.2}$$

Using the weight of the lens (15 grams) and the spring constant in the x-direction (k_x = 369 N/m), the resonant frequency value f_m is equal to 25 Hz. This frequency value can be considered to be quite below the average resonant frequency levels for convenient actuator-based applications, where most of these structures are formulated to obtain above a 100 Hz resonant frequency. The device was decided to be designed as presented, due to the restrictions on the specifications of the device that was previously mentioned. Some other considerations were that the oscillations on the device were observed to cause significant issues with stability and keeping the coil-magnet distance at a certain level for the beam-steering process. Hence, it can be stated that the flexure can be re-designed to achieve a faster scan rate at the expense of a diminished scan range in distance. It would also be desirable to increase the resonance to make the scanner tolerant to environmental vibrations.

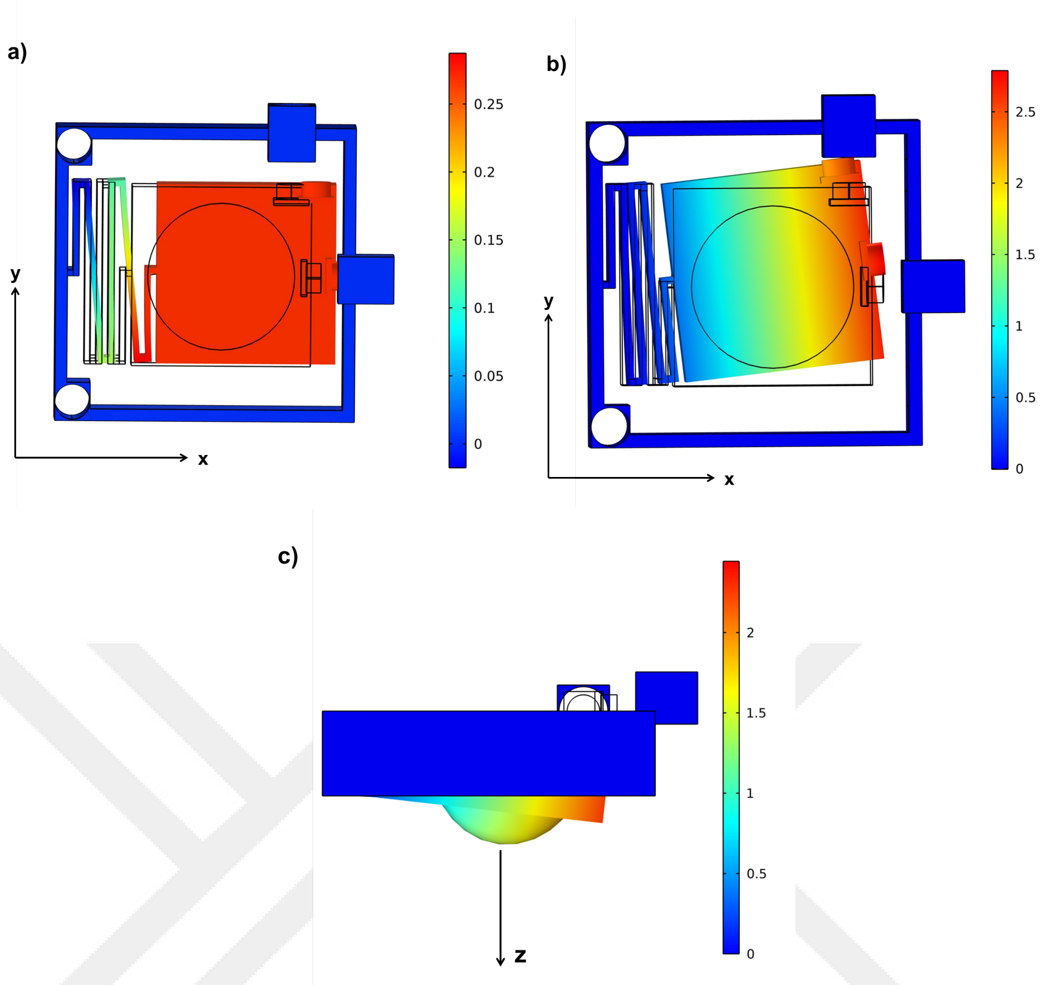

Figure 2.2 : Static deflection simulations (in mm) of the actuator in the a) x (horizontal) direction, b) y (vertical) direction, and c) z (perpendicular) direction. A force of 0.1 Newton was applied in the x and y directions, while a force of 0.15 N (corresponding to 15 grams of the total frame weight) was applied in the z-direction. The unit for the values on the color legend is N/m, which comes from the applied force over the displacement value that is caused by the load.

2.2.2 The FEA simulation for the von Mises stress

It can be stated that for the stability of the designed actuator, the stress and strain values are quite important, regarding any possible deformations or fractures in the structures with different materials of interest. The yield strength and the ultimate tensile strength are two of the most important parameters that can be considered in terms of these aspects. The yield strength of a material can be considered as a boundary value where any possible deformation can occur on the material for stress values higher than the yield strength value, where this deformation on this material can also become permanent for load values beyond the limit. Meanwhile, the ultimate tensile strength indicates the maximum load which the material can resist prior to fracture. The von Mises stress is therefore used to determine whether the provided structure, which consists of the material of interest, will yield or fracture depending on the load.

The FEA simulation for the von Mises stress on the flexure of the actuator is presented in Figure 2.3. As the material of interest in this design is PLA, the yield strength value is considered to be approximately 26.082 MPa, while the ultimate tensile strength value is approximately 32.938 MPa [24]. Meanwhile, the FEA simulation reveals that the sag due to gravity causes a maximum von Mises stress value of 2.5 MPa, which is significantly lower than the denoted theoretical yield strength.

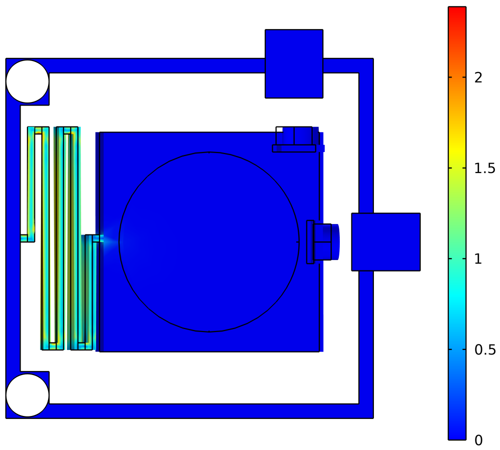

Figure 2.3 : The von Mises tensile stress simulation of the actuator. A force of 0.15 N (corresponding to 15 grams of the total frame weight) was applied in the z-direction. The unit for the values on the color legend is MPa.

The geometry of the flexure holding the lens frame dictates its spring constant in all three directions. The flexure height was kept as thick as 10 mm to increase the spring constant (k_z) in the z-direction. Adjusting the flexure height to a higher value would indeed result in lower sag due to gravity while compromising its steering capability. Alternatively, manufacturing the springs with a slight tilt or utilizing a lightweight lens (i.e. a Fresnel lens) will compensate for or mitigate the sag.

2.3 Fabrication of the Actuator

After these specifications regarding the designed actuator, some details about the fabrication process of the actuator will be provided. The CAD drawings, which were created in AutoCAD, were converted to an STL (Standard Triangle Language) file. These files are used to describe the design of the model using triangular surfaces defined by the three-dimensional Cartesian coordinate system. The STL files are therefore used to prepare the formulated 3D model of the actuator for the 3D printing process. The STL file of the actuator is then sent to the Ultimaker Cura 3D printing software. In Cura, the design of interest is converted to a G-code file, which is used to configure the 3D printer with the necessary information about the three-dimensional coordinates of the dimensions and content of the model.

Table 2.2 : The 3D printing settings parameters for the designed actuator, conducted with the Creality Ender-3 Pro 3D printer.

Parameter	Value
Layer Height	0.12 mm
Wall Thickness	0.3 mm
Wall Line Count	1
Top and Bottom Thickness	0.3 mm
Top and Bottom Layer Count	3
Infill Density	%15
Infill Pattern	Lines
Printing Temperature	217 °C
Build Plate Temperature	57 °C
Print Speed	40 mm/s

The designed actuator was fabricated with the Creality Ender-3 Pro 3D printer, using the Fused Deposition Modeling (FDM) technique. The fabrication process was conducted with a nozzle size of 0.3 mm and PLA was used as the material in the fabrication of the actuator. Some information about the print settings parameters, for the final version of the actuator, is provided in Table A.8. These parameters are configured for the prepared G-code file in the interface of Cura. These parameters were also regularly changed and re-configured in order to address definite faults and occurrences during and after the printing process. Hence, after specific changes and improvements in the design of the actuator and the printing process were concluded, the final prototype was fabricated in approximately 4 hours and 25 minutes.

2.4 Experimental Setup

The manufactured actuator was attached to the ceiling of our miniaturized VLC test-bed (70 cm x 40 cm x 40 cm cardboard box setup with 4 LEDs inserted to its ceiling in Cartesian fashion with 20 cm distance, and an additional LED at the center) via two 6-mm diameter cage rods inserted into the corner holes of the outer frame of the actuator, as well as the cardboard ceiling (Figure 2.4). The lens was adjusted to be approximately 27 mm away from the center LED to obtain the designated focus at the base. The beam steering can be characterized by observing the shift of the focused beam with respect to voltage (or current) applied to the coils with a CMOS camera or by observing the focused spot on a piece of graph paper on the test-bed floor while the camera is placed elsewhere to image the spot location (which is particularly useful when the displacement of the focused beam spot is larger than the camera sensor area). Finally, a proof-of-principle physical secure communication demonstration is conducted, where a legitimate target is tracked with a camera and the observed location is used to steer the beam on the moving target (Figure 2.4.c).

A face recognition routine was implemented using OpenCV and the face recognition libraries of Python. The code uses a legitimate target (the printed photograph of Albert Einstein) as the input dataset. The code compares the facial features contained in the input dataset with a sample open-source dataset that contains Haar-like features based on the images of different targets. Once recognized, the target of interest is detected, and a square is drawn around the face whose corners are used as coordinate feedback for the actuator. The coordinates are then converted to voltages via a linear operation (shown with a triangle in Figure 2.4.b) on the live video feed.

2.4.1 The optical setup of the experiment

The optical setup of the experiment that depicts the LED, actuator and the changes in the image (lens-focal spot) distance due to the displacements conducted by the electromagnetic actuation from the coils and magnets is depicted in Figure 2.5. During the actuation process, the sag itself causes the highest amount of focal change. Hence, the initial distance between the LED and the lens should be set, accounting for the static sag. On top of the sag, the beam steering device can be actuated for a 1 mm distance in both x and y-directions. Using the imaging equation:

$$\frac{1}{f} = \frac{1}{d_I} + \frac{1}{d_O} \qquad \textbf{(2.3)}$$

where f is the focal length of the lens, d_I and d_O are the image (lens-focal spot) and object (LED-lens) distances, respectively. When the device is actuated by an amount of d_x in the x-direction and d_y (not depicted in figure) in the y-direction, the object distance can be updated as:

$$d'_O = \sqrt{d_O^2 + d_x^2 + d_y^2} \qquad \textbf{(2.4)}$$

Using Equations 2.3 and 2.4, and assuming $d_x = d_y = 1$ mm, $d_O = 27$ mm, the beam-steering causes the imaging distance to decrease from $d_I = 37.2$ cm to $d_I' = 36.5$ cm. The change in the focal length is well within the depth-of-focus (DOF) of the imaging system. Thus, the focal shift is not on the order to impact the gains provided by the lens steering actuator.

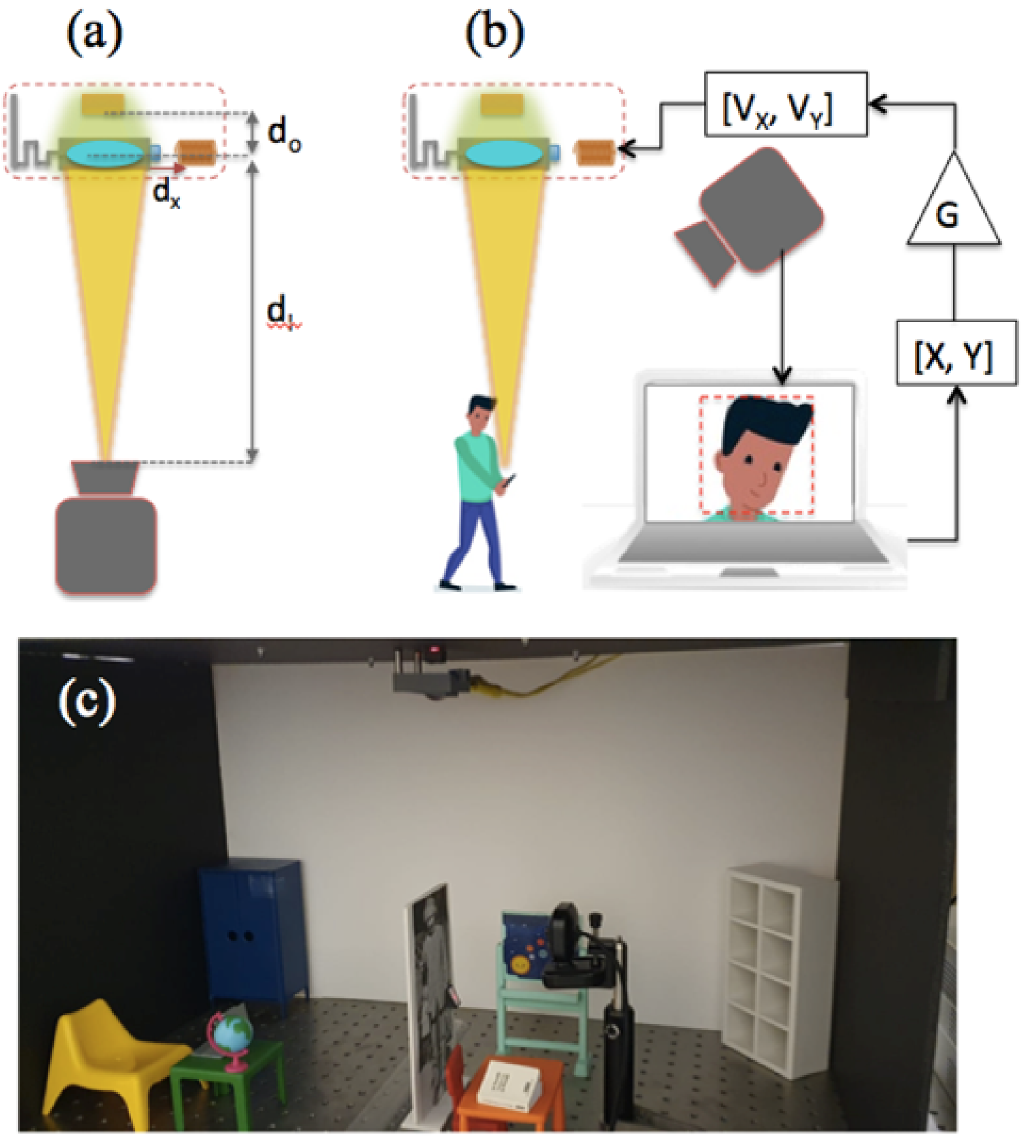

Figure 2.4 : Experimental setup; a) for characterizing coil voltage (or current) vs. scan line b) beam steering using location information from the face-recognition routine, where corner pixel values of the dashed square is converted to coil drive voltages. c) The test-bed; showcasing the VLC test-bed with the integrated actuator, a legitimate receiver (Einstein) and an external camera for face recognition and position feedback.

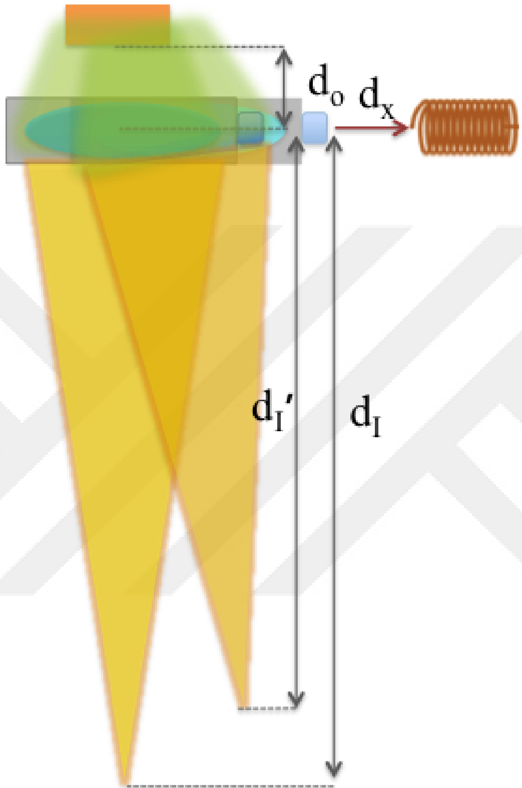

Figure 2.5 : The optical setup of the experiment, which depicts the coil-magnet distance (d_x), the object (LED-lens) distance (d_O) and the image (lens-focal spot) distance that changes due to the displacements facilitated by the electromagnetic actuation. The initial image distance value is denoted with d_I and the changed distance value is denoted with d_I'.

3. EXPERIMENTAL RESULTS

In this chapter, the results and demonstrations of the optical beam-steering experiment using the designed actuator are provided and depicted in the sections below.

3.1 Voltage vs. Displacement Measurement Results

Firstly, the deflection of the focused spot on the test-bed base can be observed as a function of voltage, as presented in Figure 3.1. A displacement of 12 mm is established with 10 V applied voltage (70 mA current) for both axes, corresponding to nearly 900 µm displacement of the actuator in both directions based on the optical magnification of the system (1:13.5). It was observed that with the lens scanner, the focused LED light can be steered with an average displacement per voltage value of 1.33 mm/V in the x (horizontal) direction and 1.226 mm/V in the y (vertical) direction. It is noteworthy to mention that the scan length can be directly improved upon the use of a miniaturized and higher NA lens to obtain a much larger optical magnification. The steering range can further be improved by the use of higher drive voltages, at the expense of higher power consumption.

The provided result for the measurement of the horizontal and vertical displacement per voltage was chosen as the one with the largest values out of all the experiments that were conducted. More details regarding the comparison of this result with the other experiments based on the nominal and the average horizontal and vertical displacement per voltage values are described in Appendix A.

3.2 Demonstrations of Beam-Steering on CMOS Camera

Next, using the setup illustrated in Figure 2.4, the LED beams are steered onto the CMOS camera (Thorlabs 1501M) using the actuator. The light intensity was observed for four adjacent locations. In the meantime, a hypothetical scenario is tested where the legitimate receiver walks through adjacent locations while illegitimate receivers occupy the rest of the locations, as illustrated in Figure 3.2.

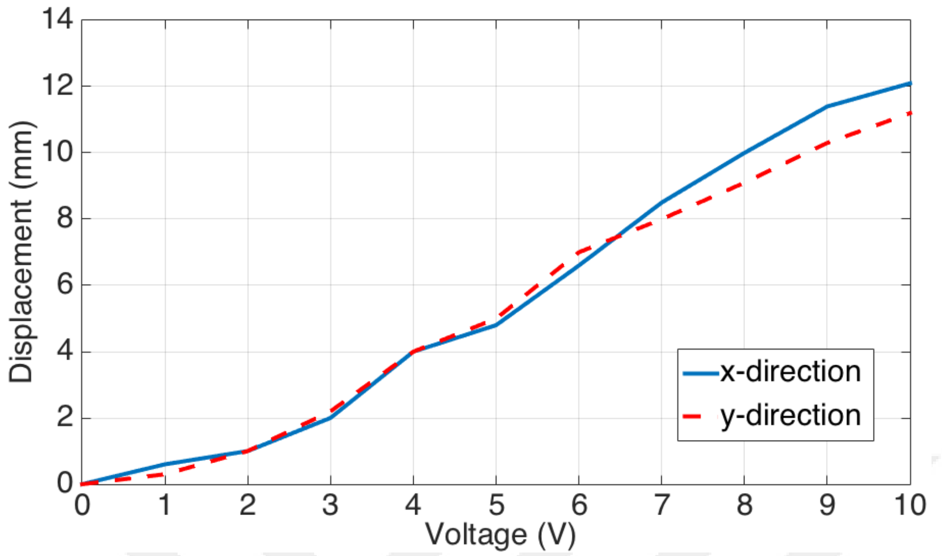

Figure 3.1 : The measurement results, displaying the displacement of the focused LED as a function of applied voltage.

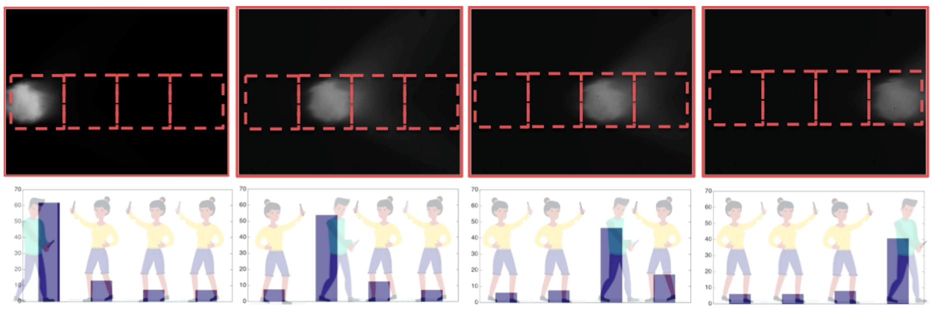

Figure 3.2 : Beam-steering on CMOS camera. The bar graphs show amount of average CCD intensity values.

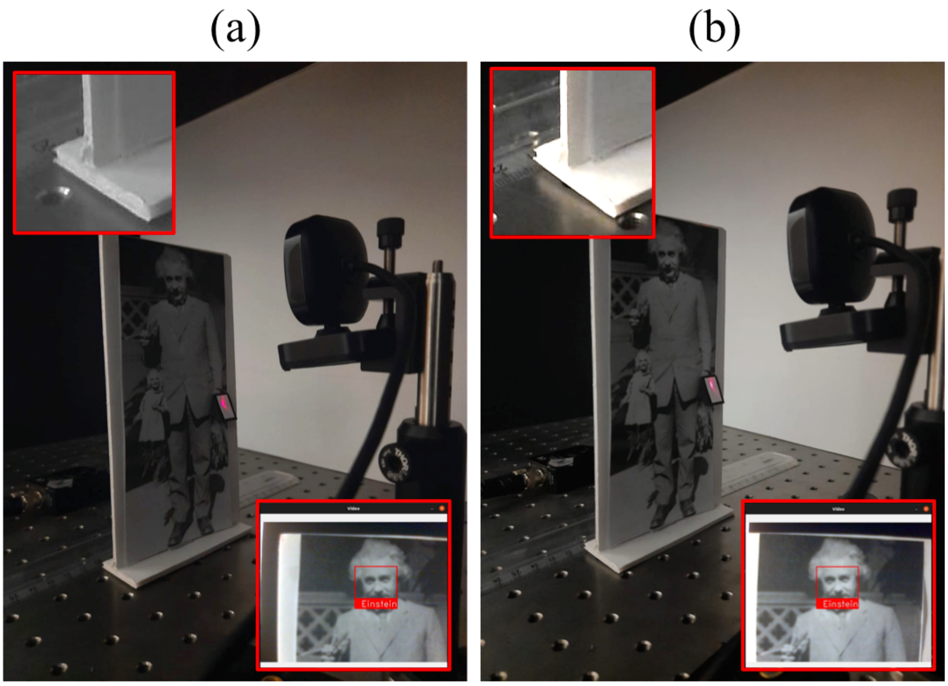

Figure 3.3 : Demonstration of beam-steering a) original position of the target (ruler set at 20 cm) and b) target moved left by 1 cm (ruler set at 21 cm). Insets show the magnified location of the target and face recognition screen.

The presented actuator steers the beam onto the legitimate receiver while LEDs within the test-bed are also turned ON. Figure 3.2 illustrates the average intensity levels (averaged over square slots) received by legitimate and illegitimate receivers, showcasing significantly lower light intensities than the legitimate receiver. It can be noted that the lateral offset (during the steering process) between the LED and the actuator caused a slight change in the intensity level received by Bob.

3.3 Demonstrations of Beam-Steering through Face Recognition Feedback

Finally, the last experiment involved the demonstration of tracking of the Einstein target based on face recognition feedback (Figure 3.3). As previously mentioned, the pixel location of the square center (or corner) is converted to the drive voltage of the coil via a linear relationship. Moving the target by 1 cm resulted in an 80-pixel shift of the detected face. Thus, the application of a 0.11 V/pix shift of the detected face coordinate (totaling approximately 9 V for 1 cm movement) results in successful steering for the presented experimental conditions and actuator. The steering drive voltage and current values can be separately pre-calibrated for both axes on any given lens scanner device.

4. DISCUSSION

In this chapter, the discussion section regarding the secrecy improvement in the depicted VLC system through the demonstrated physical layer security scheme is presented. In the meantime, the upscaling of the proposed system to real-world dimensions is also discussed. Lastly, some information regarding the improvements to the design of the actuator based on the observations during the fabrication and experiment phases is also provided, along with a discussion on the possible plastic deformation observed on the actuator due to the configured low infill rate.

4.1 The Improvement in the Secrecy Capacity

In this section, the improvement in the secrecy capacity of this VLC system through the use of a lens scanner is demonstrated. Figure 4.1 illustrates Bob and Eve, where the focused emitter targets (and follows) Bob, while Eve is underneath a light source without a focusing mechanism. The signal-to-noise (SNR) of both Bob and Eve can be compared under a number of assumptions that are summarized in Table 4.1.

Table 4.1 : The parameters used in calculating the SNR of the scenario sketched in Figure 4.1.

Parameter	Value
LED Power *	5 mW
LED half angle *	14°
Photo-detector (PD) noise **	5.8 pW/Hz$^{1/2}$
Bandwidth (BW) *	1 MHz
Photo-detector radius *	1.8 mm
PD Gain *	2.38 kV/A
Responsivity ***	0.4 A/W

* Thorlabs 600L

** for Thorlabs PDA36A2 trans-impedance amplified (TIA) photo-detector

*** for red (= 600 nm) light source

A number of noise sources (i.e. Johnson, Shot, Flicker, light intensity fluctuation [25]) determine the noise floor of the photo-detector units carried by Bob and Eve. In the

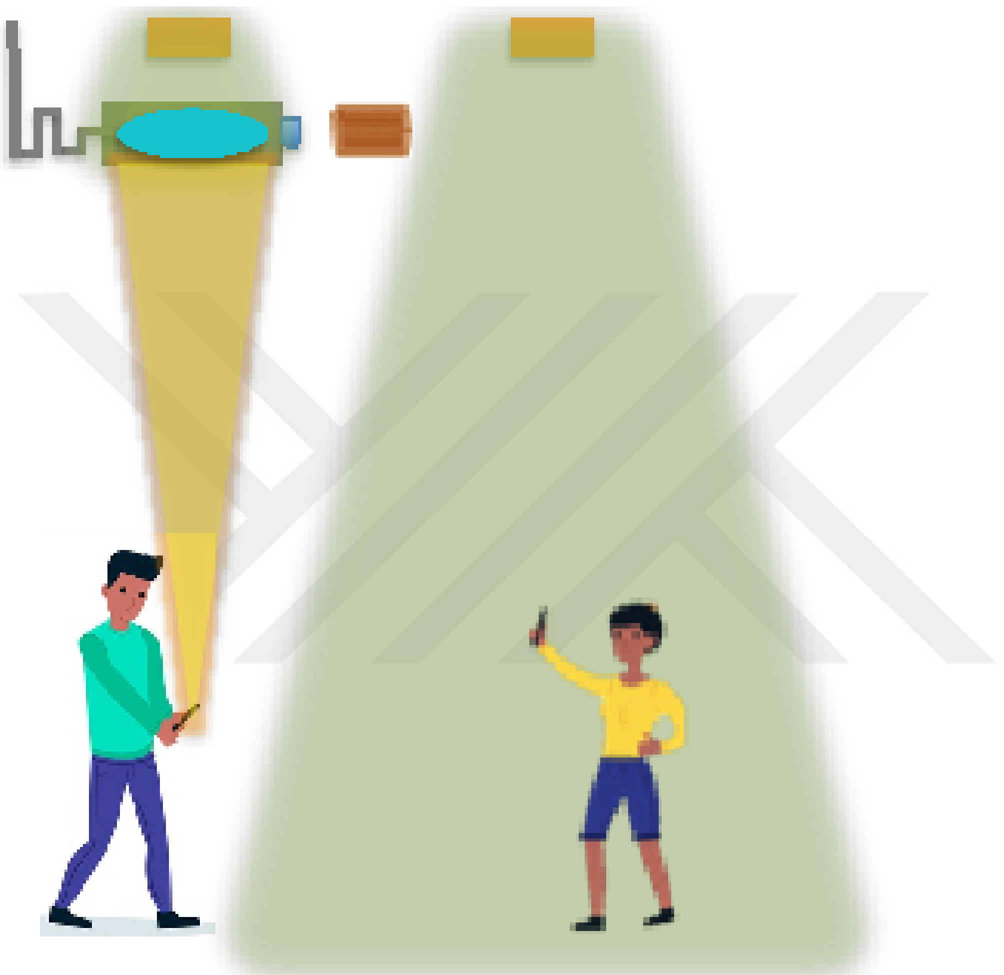

Figure 4.1 : An exemplary sketch of secrecy improvement, where Bob is targeted by the steerable focused emitter (with the lens scanner) and Eve is underneath a conventional (non-focused) emitter.

provided SNR calculation, the LEDs (one of them above Bob, and the other above Eve) are considered to have P_0 = 5 mW optical power and a noise-equivalent power (NEP) of 5.8 pW/Hz$^{1/2}$ for the photo-diode and trans-impedance amplifier (Thorlabs PDA36A2). Then, Bob will receive nearly all of 5 mW (given that the lens numerical aperture is greater than the light numerical aperture, the lens is anti-reflective layer coated, and the photo-detector dimension encompasses the focused light spot), as the emitted light from the LED is mapped to Bob. On the other hand, without a focused LED, the light spot diverges to R_L = 10 cm radius at the bottom surface of the miniaturized test-bed. Assuming a Gaussian light distribution, the power received by a finite-sized detector (R_D = 1.8 mm for Thorlabs PDA 36A2 photo-detector) at the Eve site can be expressed as [26]:

$$P_{\mathrm{Eve}} = P_0 \frac{(R_D^2)}{(R_L^2)} \int_0^{\mathrm{R_D}} e^{\frac{-(2r^2)}{(R_L^2)}} 2\pi r * dr = P_0(1 - e^{\frac{-(2R_D^2)}{(R_L^2)}}) \qquad \textbf{(4.1)}$$

The integration of a lens scanner to target Bob effectively diminishes the focused light spot to below the size of the detector, while Eve catches a small fraction of the light without a focusing mechanism. In Figure 4.2, the optical powers for Bob and Eve are demonstrated, along with the NEP for the SNR comparison. Based on Equation 4.1 and the parameters depicted in Table 4.1; P_{Eve} = 3.24 μW, P_{Bob} = 4.3 mW (assuming that the focused spot 1/e^2 radius is equal to the detector radius) and the noise power is calculated as P_n = 58 nW. In this regard, the SNR values are calculated as 74138 (48.7 dB) and 55.86 (17.5 dB) for Bob and Eve, respectively. The secrecy capacity (C_S) can then be expressed as:

$$C_S = log_2(1 + (SNR)_{Bob}) - log_2(1 + (SNR)_{Eve}) \qquad \textbf{(4.2)}$$

The secrecy capacity is calculated to be C_S = 10.35 bits/sec/Hz, based on the scenario depicted in this section. The obtained secrecy capacity compares favorably over other literary studies on secure communications, exploiting transmit beam-forming [18], combined zero-forcing and robust beam-forming [27], optical jamming [28], spatial modulation using greedy selection [29] and deep reinforcement learning-based beam-forming [30].

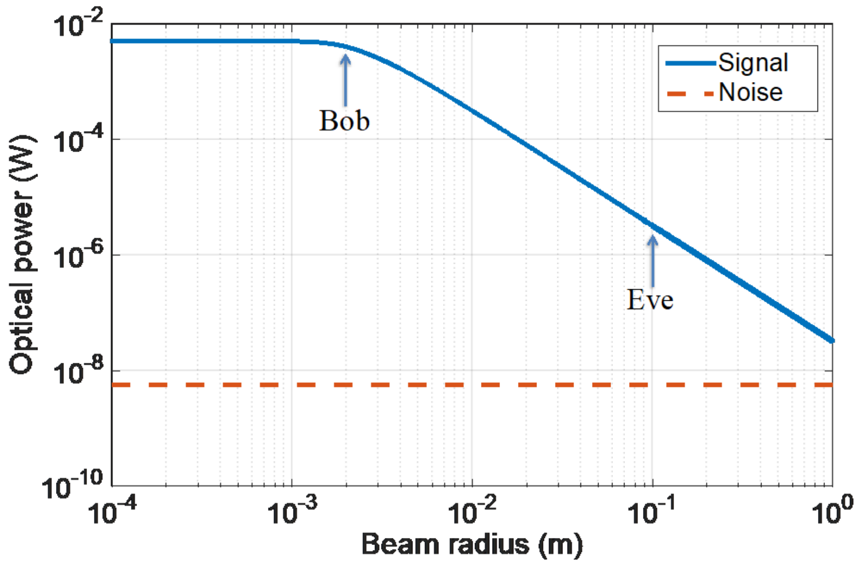

Figure 4.2 : The optical power values received by Bob and Eve in comparison to the photo-detector NEP, for the proposed scenario.

4.2 Up-scaling the Actuator to Real-World Dimensions

The adaptation of the proposed system to real-world dimensions necessitates the use of alternative lenses. The use of a f = 25 mm lens in the miniaturized room has led to an object (LED-lens) distance of d_O = 27 mm and an image (lens-focus) distance of d_I = 372 mm, in accordance with the imaging equation (Equation 2.3). The magnification ($M = d_I/d_O$) of the system in its current form is M = 14 and leads to a beam-steering capability of 12 mm (corresponding to 2 degrees of the total steering angle) under 10 Volts of drive voltage. The steering angle can be found through the inverse sine of the displacement (horizontal or vertical) divided by the image distance. Instead, integrating miniaturized lenses in the actuator (i.e. f = 2 mm lens, available in the form of molded plastic lenses in a variety of manufacturers and vendors) leads to d_O = 2.001 mm and d_I = 4 meters. The magnification of the system becomes M = 2000 and highlights a beam steering capability of nearly 2 meters (corresponding to 26 degrees of the total steering angle) under 10 V of drive voltage. An array of these devices would address a larger area for the legitimate receiver, yet should only be implemented on a portion of the LEDs in the room, so as not to hamper the lighting system's ability to properly illuminate the room. Alternatively, the electromagnetic force between the magnet and the coil can also be increased through the use of a higher inductance coil or a larger magnet. Overall, the increased actuation force would loosen the constraint on the number of actuators that should be placed in the room.

4.3 Improvements in the Actuator Prototype Through Different Designs

In order to formulate the final result for the actuator prototype, several different types of designs were used and experimented with. This was conducted in order to explore the durability of the actuator and to observe how it functions and addresses the displacements caused by the electromagnetic interactions of the coils and the magnets. For these purposes, the actuator prototype underwent many improvements that are related to the failures experienced in the previous versions during the fabrication and demonstration processes. These versions of the actuator are presented and briefly discussed in Appendix B, regarding their own features and deficiencies.

4.4 Possible Deformations on the Actuator Prototype

It can be said that while the last actuator prototype can be regarded as durable, it is also observed that it is prone to deformation after a certain amount of time. The collimating lens used in the experiment, which was placed on top of the actuator structure, was observed to apply a certain stress value on the actuator that appeared to cause a certain amount of plastic deformation on the flexure structure after one month.

It can be said that this result was caused by the low infill rate for the final prototype of the actuator structure. The weight of the collimating lens was the reason for the occurrence of mechanical fatigue and the gradual distortion of the flexure structure. Earlier, the maximum von Mises tensile stress observed in the simulation of the designed actuator was found to be 2.5 MPa, while the yield strength of PLA at %100 infill rate was taken as 26.082 MPa [24].

The stated values show that the material should yield under these circumstances. However, it was observed that flexure structure underwent distortion in the end. This result was inferred from the fact that the infill rate and the infill pattern are some of the 3D printing parameters that can determine the yield strength and ultimate tensile strength for different values, which can change through different configurations for PLA [31] [32]. Therefore, the low infill rate is suspected to be the main reason behind this occurrence. The results of the occurred plastic deformation are provided and discussed in Appendix C.

5. CONCLUSIONS

5.1 Concluding Remarks

In this thesis, a unique 3D-printed lens scanner that utilizes optical beam-steering for secure visible light communication in Li-Fi applications was presented. The scanner was manufactured using the FDM technique and PLA material while providing a beam-steering of 12 mm with a 10 V drive voltage in a 10:1 miniaturized (70 cm x 40 cm x 40 cm) VLC test-bed. The 3D-printed lens scanner was located on top of the test-bed across from the center LED, which was tested for its beam-steering capability on a moving target with face recognition feedback. The proposed physical layer security scheme leverages the significantly improved secrecy provided by focused emitters in VLC to moving targets. The calculated secrecy capacity for the proposed system compares favorably to a number of jamming, spatial modulation, and beam-forming alternatives.

5.2 Future Work

In further future work, the size of the actuator can be up-scaled for real-life applications (to map larger illumination units and to improve the scan range). The presented actuator can be used with larger room dimensions, yet up-scaling to larger illumination units will also require the use of lenses having smaller foci, to address a larger total steering angle.

REFERENCES

[1] **Nayak, A.**, **Parui, K.**, **Sharma, S. and Ratha, S.** (2020). Study and Analysis of Atomic Spectra, *International Journal of Scientific and Research Publications (IJSRP)*, *10*, 946.

[2] **Cailean, A.M. and Dimian, M.** (2017). Current challenges for visible light communications usage in vehicle applications: A survey, *IEEE Communications Surveys amp; Tutorials*, *19*(4), 2681–2703.

[3] **Kim, S.M. and Lee, H.J.** (2014). Visible light communication based on space-division multiple access optical beamforming, *Chinese Optics Letters*, *12*(12), 120601–120604.

[4] **Arnon, S.** (2015). *Visible Light Communication*, Cambridge University Press.

[5] **Khan, L.U.** (2017). Visible light communication: Applications, architecture, standardization and research challenges, *Digital Communications and Networks*, *3*(2), 78–88.

[6] **Wang, F.**, **Wang, Z.**, **Qian, C.**, **Dai, L. and Yang, Z.** (2015). Efficient vertical handover scheme for heterogeneous VLC-RF Systems, *Journal of Optical Communications and Networking*, *7*(12), 1172.

[7] **Mahmood, Z.** (2019). *The internet of things in the industrial sector*, Springer International Publishing.

[8] **Aftab, F.**, **Ulfat Khan, M.N. and Ali, S.** (2016). Light fidelity (Li-Fi) based indoor communication system, *International journal of Computer Networks amp; Communications*, *8*(3), 21–31.

[9] **Singh, J.**, **Jaiswal, S.**, **Jain, M.**, **Pathy, A.**, **Bhadoria, V. and Sharma, K.**, (2022). Li-Fi: Future of Wireless Technology, pp.798–805.

[10] **Blinowski, G.** (2015). Security Issues in Visible Light Communication Systems, *IFAC-PapersOnLine*, *48*(4), 234–239.

[11] **Shannon, C.E.** (1949). Communication theory of secrecy systems*, *Bell System Technical Journal*, *28*(4), 656–715.

[12] **Wyner, A.D.** (1975). The wire-tap channel, *Bell System Technical Journal*, *54*(8), 1355–1387.

[13] **Dong, L.**, **Han, Z.**, **Petropulu, A. and Poor, H.** (2010). Improving wireless physical layer security via cooperating relays, *IEEE Transactions on Signal Processing*, *58*(3), 1875–1888.

[14] **Eghbal, M. and Abouei, J.** (2014). Security enhancement in free-space optics using acousto-optic deflectors, *Journal of Optical Communications and Networking*, *6*(8), 684.

[15] **Panayirci, E.**, **Yesilkaya, A.**, **Cogalan, T.**, **Poor, H.V. and Haas, H.** (2020). Physical-layer security with optical generalized space shift keying, *IEEE Transactions on Communications*, *68*(5), 3042–3056.

[16] **Cho, S.**, **Chen, G. and Coon, J.P.** (2018). Securing visible light communication systems by beamforming in the presence of randomly distributed eavesdroppers, *IEEE Transactions on Wireless Communications*, *17*(5), 2918–2931.

[17] **Mostafa, A. and Lampe, L.** (2015). Physical-layer security for miso visible light communication channels, *IEEE Journal on Selected Areas in Communications*, *33*(9), 1806–1818.

[18] **Mostafa, A. and Lampe, L.** (2016). Optimal and robust beamforming for secure transmission in miso visible-light communication links, *IEEE Transactions on Signal Processing*, *64*(24), 6501–6516.

[19] **Çirkinoğlu, H.O.**, **Ferhanoğlu, O. and Karabulut Kurt, G.** (2021). Improved physical layer security of visible light communications with focused light emitters, *Optics Communications*, *485*, 126752.

[20] **Gürcüoğlu, O.**, **Derman, I.D.**, **Altınsoy, M.**, **Khayatzadeh, R.**, **Çivitci, F.**, **Erten, A.C. and Ferhanoğlu, O.** (2021). A 3D-printed 3D actuator for miniaturized laser scanning probes, *Sensors and Actuators A: Physical*, *317*, 112448.

[21] **Bargiel, S.**, **Nieradko, L.**, **Józwik, M.**, **Gorecki, C. and Dziuban, J.A.** (2006). New generation of fully integrated optical microscopes on-chip: Application to confocal microscope, *SPIE Proceedings*.

[22] **Liu, T.**, **Rajadhyaksha, M. and Dickensheets, D.L.** (2019). MEMS-in-the-lens architecture for a miniature high-na laser scanning microscope, *Light: Science amp; Applications*, *8*(1).

[23] **Senturia, S.D.** (2004). *Microsystem Design*, Springer.

[24] **Subramaniam, S.R.**, **Samykano, M.**, **Selvamani, S.K.**, **Ngui, W.K.**, **Kadirgama, K.**, **Sudhakar, K. and Idris, M.S.** (2019). Preliminary investigations of polylactic acid (PLA) properties, *AIP Conference Proceedings*.

[25] **Hobbs, P.C.** (1997). Ultrasensitive laser measurements without tears, *Applied Optics*, *36*(4), 903.

[26] **Saleh, B.E.**, **Teich, M.C. and Masters, B.R.** (2008). Fundamentals of photonics, Second edition, *Journal of Biomedical Optics*, *13*(4), 049901.

[27] **Arfaoui, M.A.**, **Rezki, Z.**, **Ghrayeb, A. and Alouini, M.S.** (2016). On the secrecy capacity of miso visible light communication channels, *2016 IEEE Global Communications Conference (GLOBECOM)*.

[28] **Wang, F.**, **Liu, C.**, **Wang, Q.**, **Zhang, J.**, **Zhang, R.**, **Yang, L.L. and Hanzo, L.** (2018). Optical jamming enhances the secrecy performance of the generalized space-shift-keying-aided visible-light downlink, *IEEE Transactions on Communications*, *66*(9), 4087–4102.

[29] **Wang, J.Y.**, **Ge, H.**, **Lin, M.**, **Wang, J.B.**, **Dai, J. and Alouini, M.S.** (2019). On the secrecy rate of spatial modulation-based indoor visible light communications, *IEEE Journal on Selected Areas in Communications*, *37*(9), 2087–2101.

[30] **Xiao, L.**, **Sheng, G.**, **Liu, S.**, **Dai, H.**, **Peng, M. and Song, J.** (2019). Deep reinforcement learning-enabled secure visible light communication against eavesdropping, *IEEE Transactions on Communications*, *67*(10), 6994–7005.

[31] **Alafaghani, A. and Qattawi, A.** (2018). Investigating the effect of fused deposition modeling processing parameters using Taguchi design of experiment method, *Journal of Manufacturing Processes*, *36*, 164–174.

[32] **Martín, M.J.**, **Auñón, J. and Martín, F.** (2021). Influence of Infill Pattern on Mechanical Behavior of Polymeric and Composites Specimens Manufactured Using Fused Filament Fabrication Technology, *Polymers*, *13*, 2934.

APPENDICES

APPENDIX A.1 : X-direction displacement values for each experiment

APPENDIX A.2 : Y-direction displacement values for each experiment

APPENDIX A.3: Displacement values for Experiment 1

APPENDIX A.4 : Displacement values for Experiment 2

APPENDIX A.5 : Displacement values for Experiment 3

APPENDIX B.1 : Initial version of the actuator prototype - Design 1

APPENDIX B.2 : Improved version of the actuator prototype - Design 2

APPENDIX B.3: Improved version of the actuator prototype - Design 3

APPENDIX B.4 : Improved version of the actuator prototype - Design 4

APPENDIX B.5 : Improved version of the actuator prototype - Design 5

APPENDIX C.1 : Figure of the actuator, depicting the described distortion on the flexure structure.

APPENDIX C.2 : A figure that depicts the distortion on the flexure structure from a diagonal view.

APPENDIX C.3 : Another figure that depicts the distortion on the flexure structure from a diagonal view.

APPENDIX A - More Details on the Experimental Results

In this section, some of the experiments that were conducted in Chapter 3 are presented in more detail. These experiments consist of the horizontal (x-direction) and vertical (y-direction) displacement values in millimeters (mm), per drive voltage values supplied to the coils in Volts (V). Out of these experiments, three of them were chosen that can be considered to have the largest amount of displacement values per x and y-directions.

Table A.1 : The displacement per voltage values for the x-direction in Experiment 1.

Voltage (V)	Displacement (mm)
0	0
1	0.6
2	1
3	2
4	4
5	4.8
6	6.6
7	8.5
8	10
9	11.4
10	12.1

Table A.2 : The displacement per voltage values for the y-direction in Experiment 1.

Voltage (V)	Displacement (mm)
0	0
1	0.3
2	1
3	2.2
4	4
5	5
6	7
7	8
8	9.1
9	10.3
10	11.2

Table A.3 : The displacement per voltage values for the x-direction in Experiment 2.

Voltage (V)	Displacement (mm)
0	0
1	0.5
2	1.3
3	1.95
4	3.5
5	4.5
6	6
7	8
8	10
9	10.8
10	11.5

Table A.4 : The displacement per voltage values for the y-direction in Experiment 2.

Voltage (V)	Displacement (mm)
0	0
1	0.2
2	0.85
3	2.05
4	3.5
5	5
6	7
7	8
8	9
9	10.1
10	10.8

Table A.5 : The displacement per voltage values for the x-direction in Experiment 3.

Voltage (V)	Displacement (mm)
0	0
1	0.5
2	1.2
3	1.95
4	3.7
5	4.5
6	6.2
7	8
8	10
9	10.8
10	11.8

Table A.6 : The displacement per voltage values for the y-direction in Experiment 3.

Voltage (V)	Displacement (mm)
0	0
1	0.2
2	0.8
3	1.9
4	3.5
5	5
6	7
7	7.9
8	9.1
9	10.1
10	10.9

Table A.7 : The Average Displacement in the x-direction per Voltage Values

Experiment Number	Average Displacement per Voltage (mm/V)
1	1.33
2	1.267
3	1.273

Table A.8 : The Average Displacement in the y-direction per Voltage Values

Experiment Number	Average Displacement per Voltage (mm/V)
1	1.226
2	1.213
3	1.223

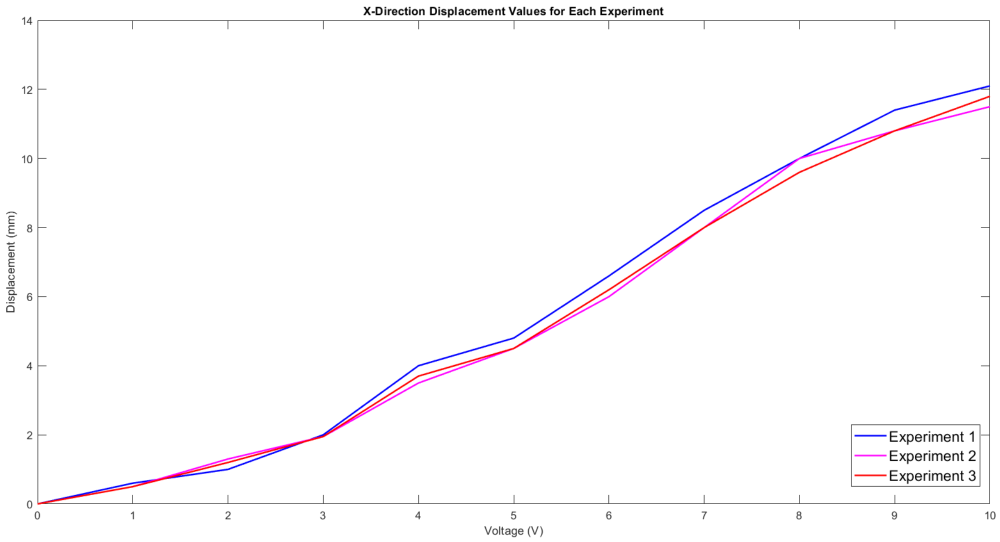

Figure A.1 : The x-direction displacement values for each experiment combined together, in order to compare the different values of increase in the horizontal displacement per voltage.

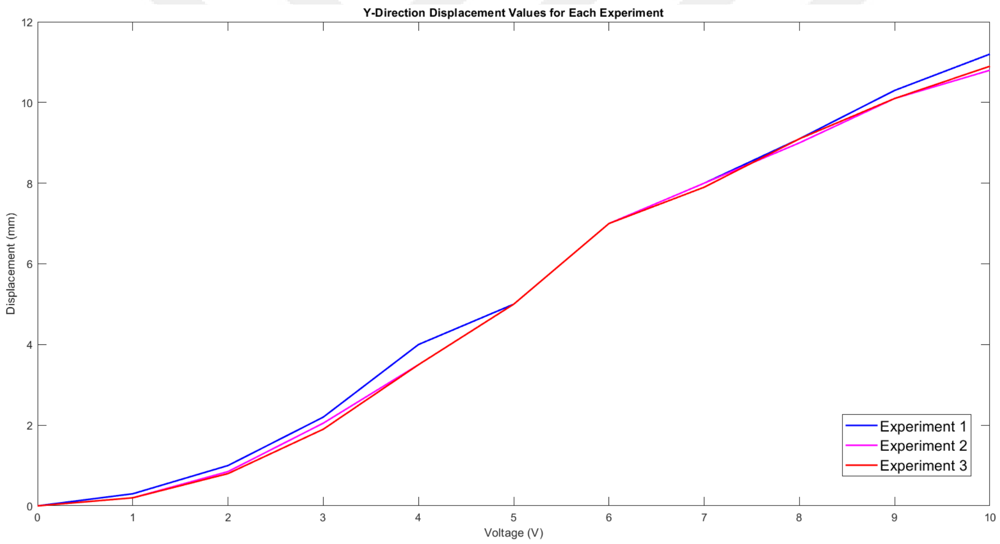

Figure A.2 : The y-direction displacement values for each experiment combined together, in order to compare the different values of increase in the vertical displacement per voltage.

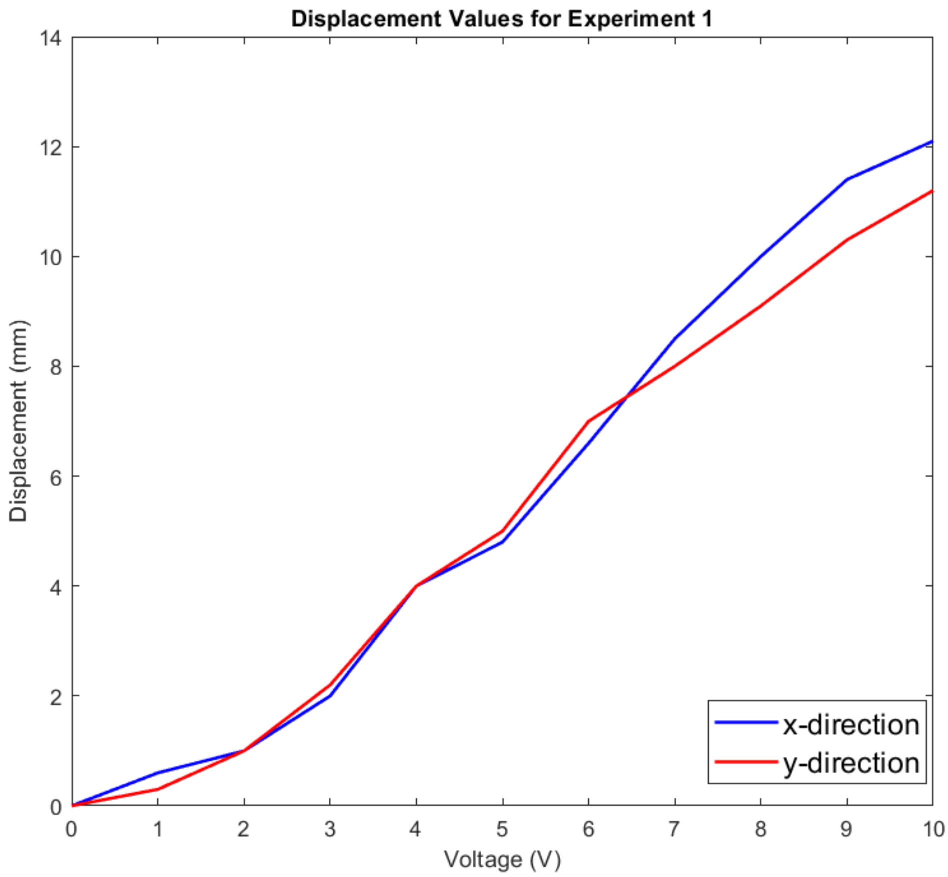

Figure A.3 : The x and y-direction displacement values for Experiment 1.

Figure A.4 : The x and y-direction displacement values for Experiment 2.

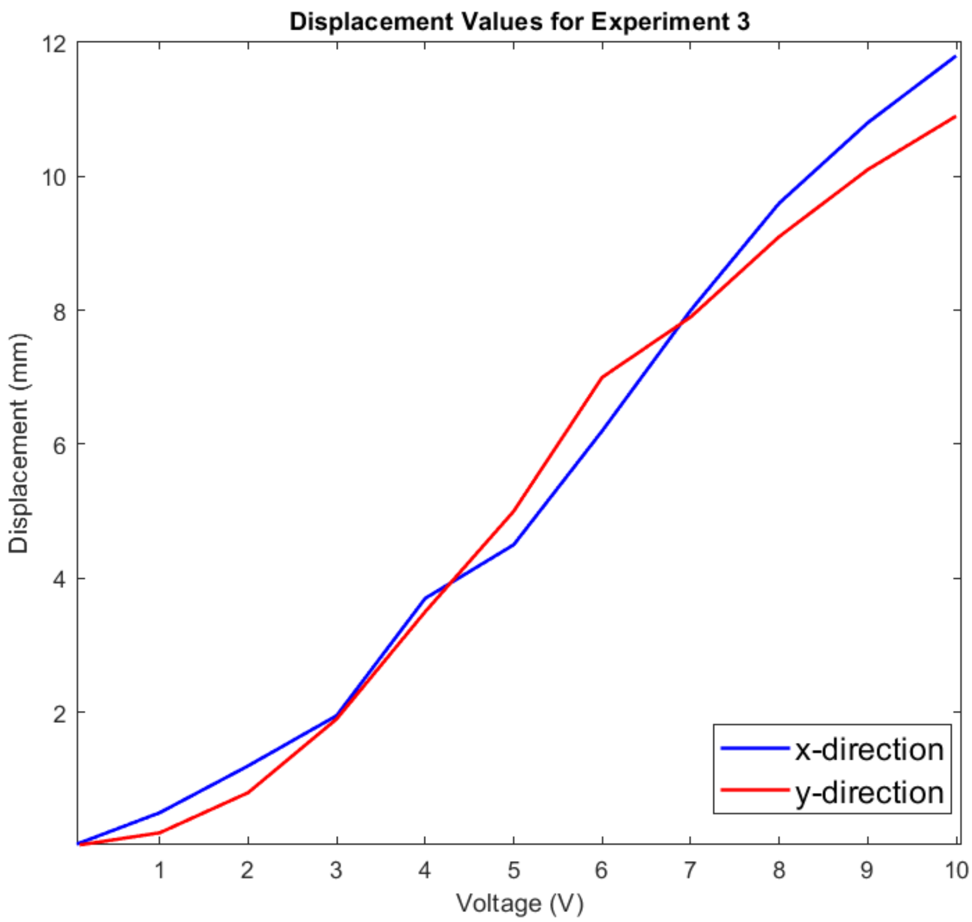

Figure A.5 : The x and y-direction displacement values for Experiment 3.

APPENDIX B - The Improvements in the Design of the Actuator

In this section, some sample figures regarding the changes and improvements in the design of the actuator in order to formulate and fabricate the final prototype are provided.

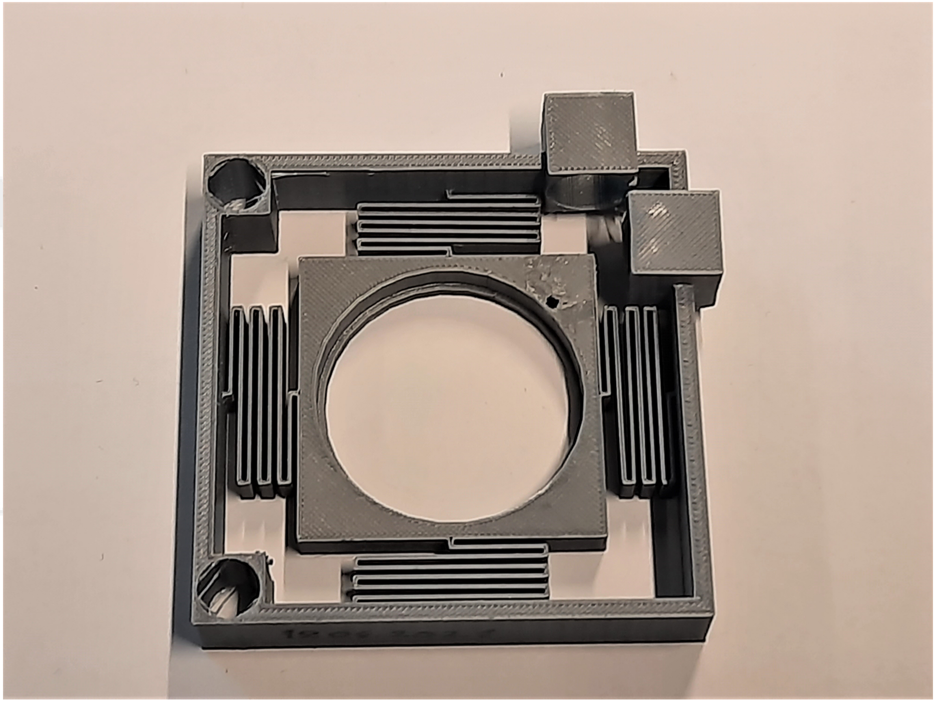

Figure B.1 : Design 1 is one of the first prototypes of the actuator. It consists of four flexures of 3T period, located at each side of the lens frame that connects it to the outer frame of the actuator. This design was formulated to test the stability of the actuator and to discover the displacements of the focused LED beam, conducted through optical beam-steering. However, this prototype was found to be inadequate to produce any displacement in x and y-directions for the optical beam-steering process, and therefore, it was dismissed.

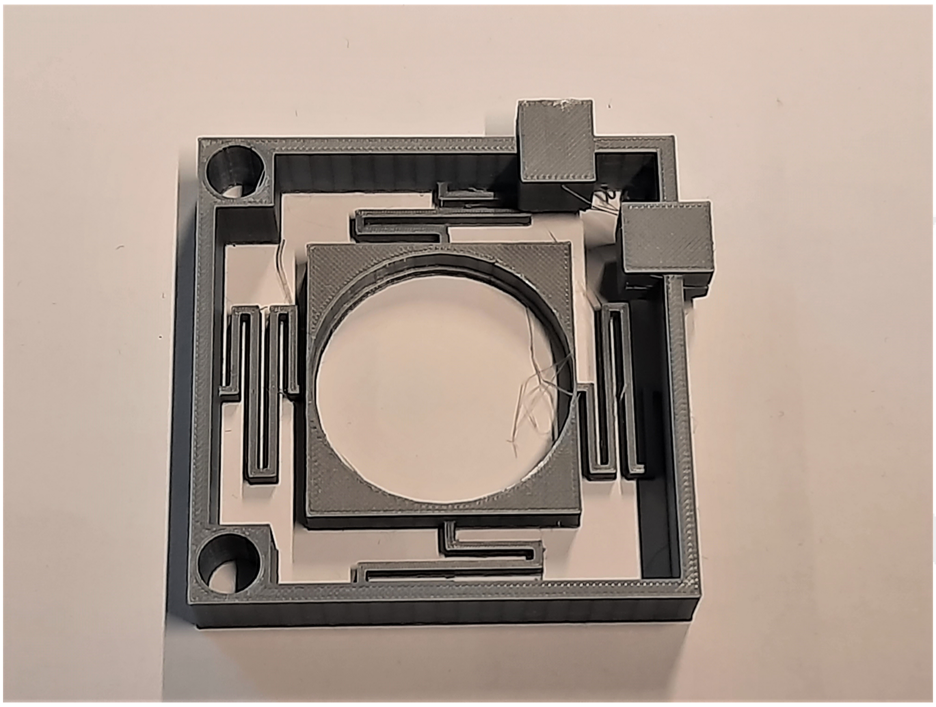

Figure B.2 : Design 2 is an improved version of Design 1, which consists of four flexures of 1.5T period, located at each side of the lens frame that connects it to the outer frame of the actuator. It was utilized to try to increase the displacement values while trying to keep the actuator stable. However, this prototype produced very low and insufficient displacement values, and therefore, it was dismissed.

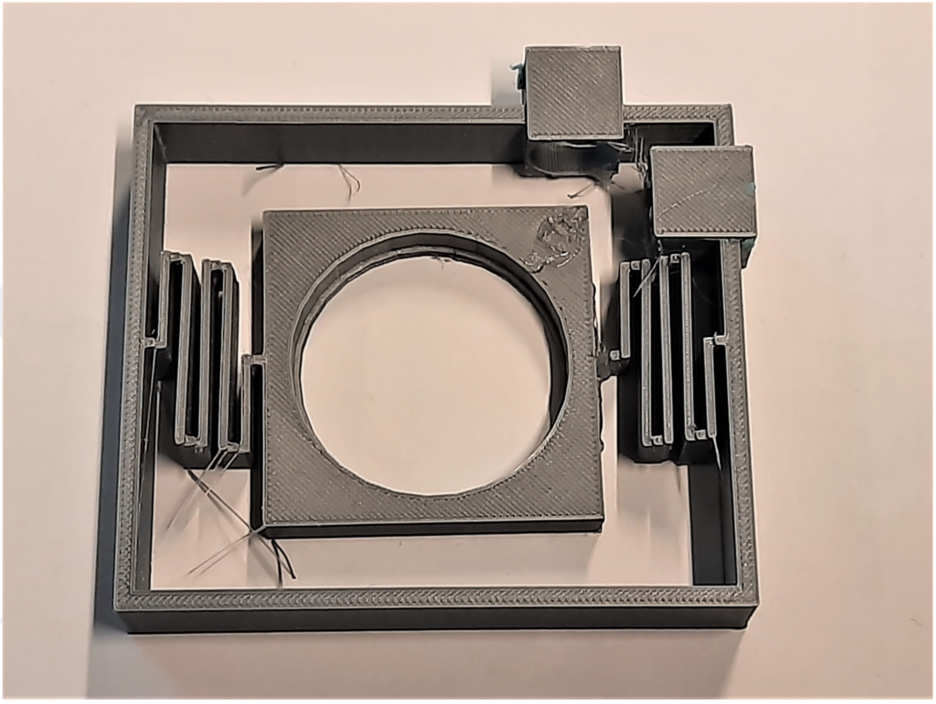

Figure B.3 : Design 3 consists of two staircase-shaped flexure structures of 2T period, located at the left and right sides of the lens frame. It was utilized to try to increase the displacement values while trying to keep the actuator stable. It was assumed that the staircase-like structure would provide stability to the lens frame and counter the additional weight caused by the lens. While the x-direction displacement result of the actuator was not really low, there was no movement in the y-direction. In the end, this design and the idea of adding flexures to two sides of the actuator were dismissed.

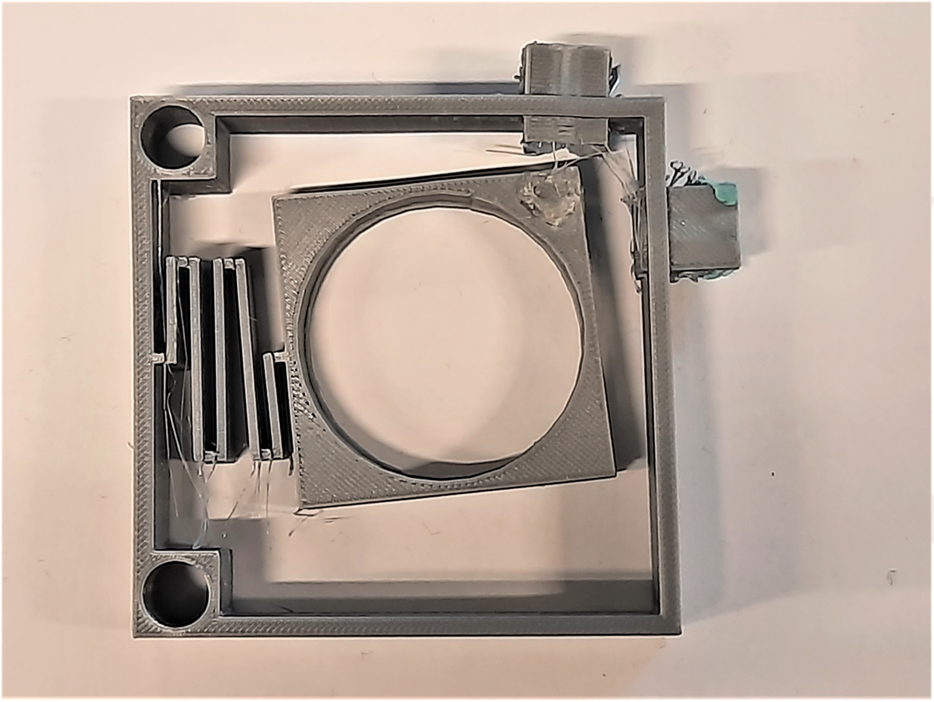

Figure B.4 : Design 4 consists of a singular staircase-shaped flexure structure of 2T period, located on the left side of the lens frame. It was utilized to try to increase the displacement values that were previously found to be insufficient. The x and y-direction displacement results were found to be better, and in the end, the idea of using only one flexure structure was carried on.

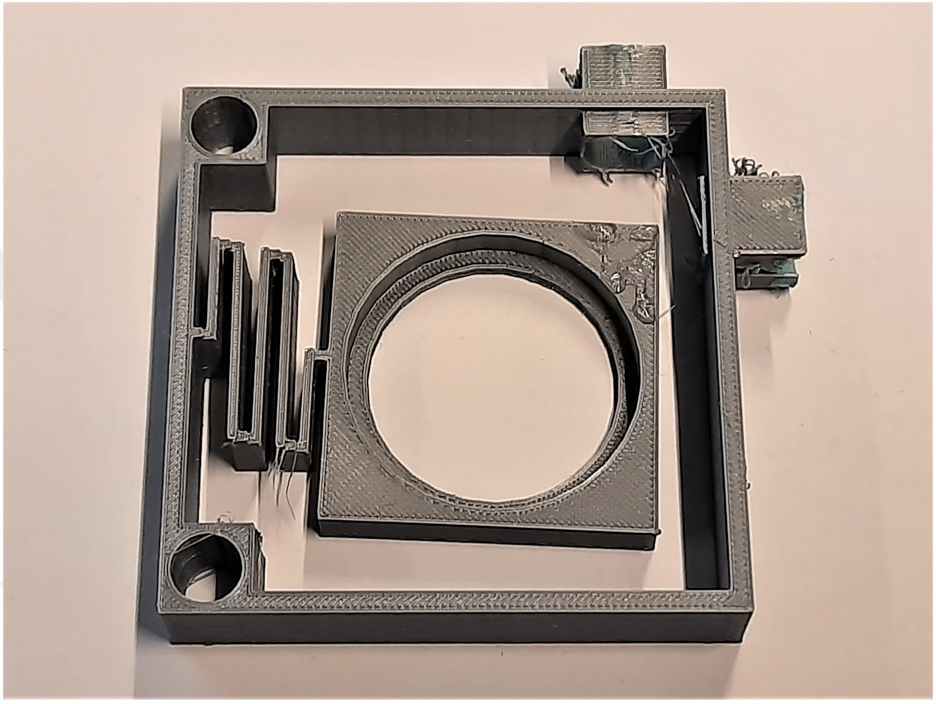

Figure B.5 : Design 5 is quite similar to Design 4. The only difference from Design 4 is that the lower part of the lens holder frame now has a smaller space. This was done in order for the actuator to be able to use different types of lenses for the experiment. After this design, the idea of using a staircase-shaped flexure structure was dismissed, and instead, a flexure structure of 2T period, with the same flexure height for every part of the structure, was utilized to formulate the final prototype in Figure 2.1.

APPENDIX C - The Observed Deformation on the Final Prototype

In this section, some sample figures, regarding the plastic deformation on the final prototype of the actuator, are provided.

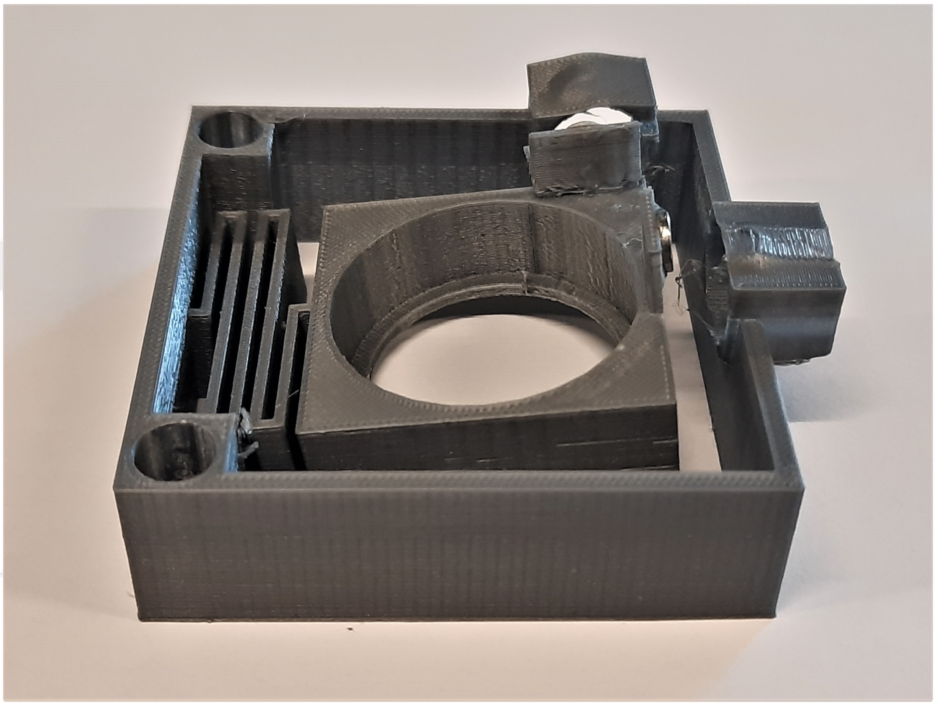

Figure C.1 : This figure shows that the flexure of the actuator structure was tilted towards the +z direction. While the actuator was being experimented on, a bulky lens was placed on the actuator that was turned upside down at one time. The structure stayed upside down and under the load from the lens for a month. Then, when the actuator structure was checked again, the result was that it underwent deformation through the occurrence of the distortion in the +z direction.

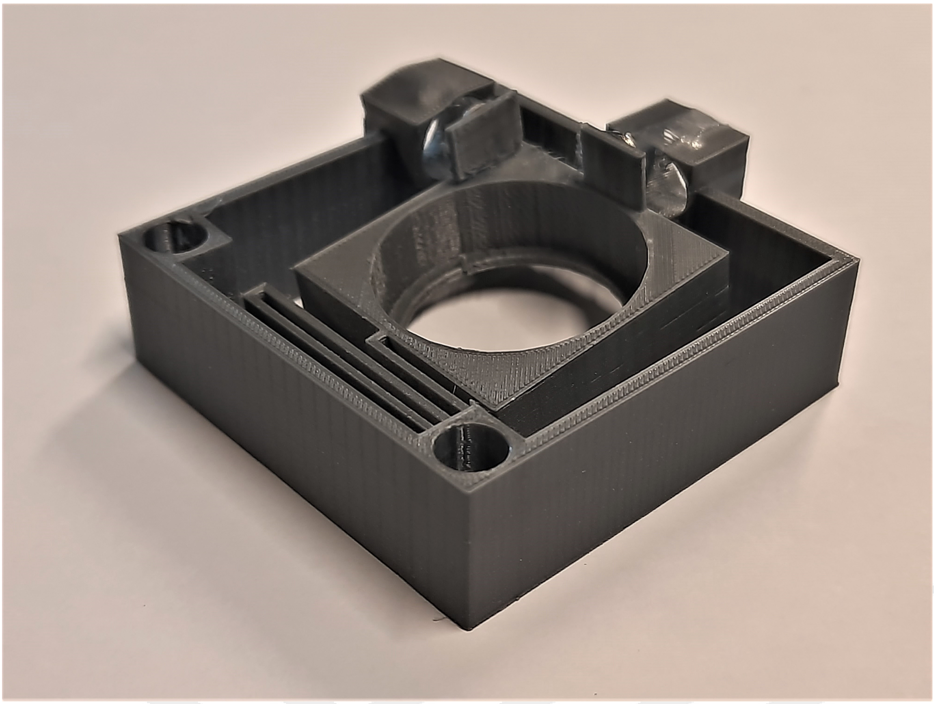

Figure C.2 : A depiction of the distortion of the flexure structure from a diagonal view.

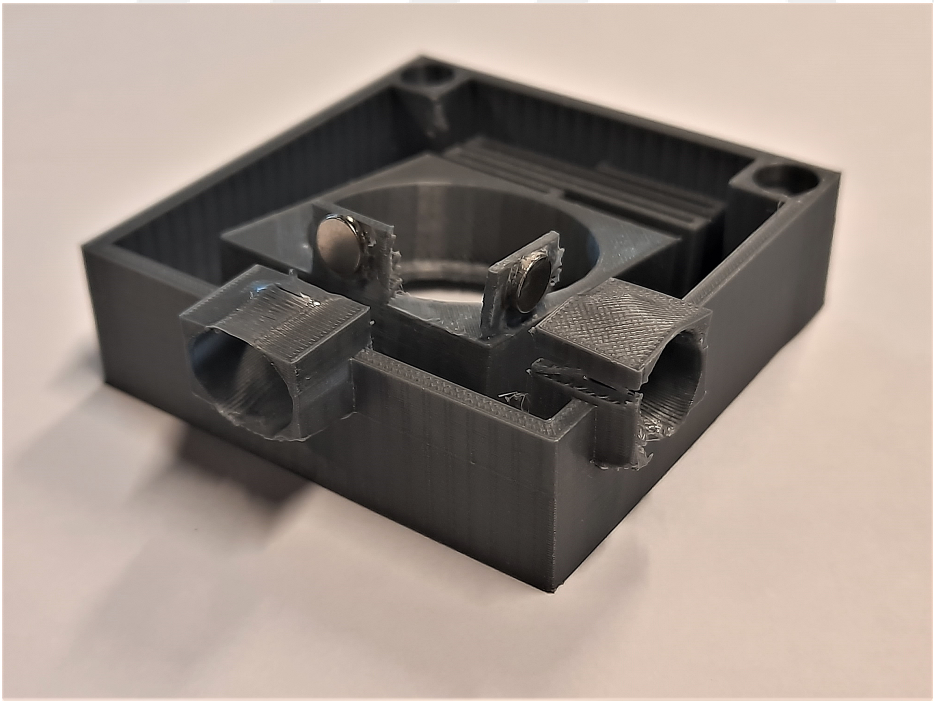

Figure C.3 : Another depiction of the distortion of the flexure structure from a diagonal view.

CURRICULUM VITAE

Name Surname : Mehmet Can ERDEM

EDUCATION :

- **B.Sc.** : 2020, Koç University, Faculty of Engineering, Department of Electrical and Electronics Engineering

PROFESSIONAL EXPERIENCE AND REWARDS:

- Participated in a TÜBİTAK project named "Physical Layer Security in Visible Light Communication", with the number 218E034, in the Electro-Optic Devices Laboratory at Istanbul Technical University between 2020 and 2021.

PUBLICATIONS, PRESENTATIONS AND PATENTS ON THE THESIS:

- **M. C. Erdem, O. Gürcüoğlu, E. Panayırcı, G. K. Kurt, and O. Ferhanoğlu.** 3D-printed actuator-based beam-steering approach for improved physical layer security in visible light communication. *Applied Optics*, 61(18), 5375–5380, 13 June 2022.

OTHER PUBLICATIONS, PRESENTATIONS AND PATENTS:

- **O. Gürcüoğlu, M. C. Erdem, O. Ferhanoğlu, E. Panayırcı, and G. K. Kurt.** Cost-effective test-bed for secure visible-light communication. *Optical Engineering*, 61(06), 064105, 13 June 2022.

- **O. Gürcüoğlu, M. C. Erdem, H. O. Çirkinoğlu, O. Ferhanoğlu, G. K. Kurt and E. Panayırcı.** Improved Physical Layer Security in Visible Light Communications by Using Focused Light Emitters. *2021 29th Signal Processing and Communications Applications Conference (SIU)*, 9-11 June 2021. Istanbul, Turkey.

M. C. ERDEM

3D-Printed Actuator-Based Beam-Steering Approach for Improved Physical Layer Security in Visible Light Communication

2022